ACS NANO

www.acsnano.org

Open Access

This article is licensed under CC-BY-NC-ND 4.0

ARTICLE

Superparamagnetic Iron Oxide Nanoparticles Reprogram the Tumor Microenvironment and Reduce Lung Cancer Regrowth after Crizotinib Treatment

Natalie K. Horvat,[▲] Sara Chocarro,[▲] Oriana Marques, Tobias A. Bauer, Ruiyue Qiu, Alberto Diaz-Jimenez, Barbara Helm, Yuanyuan Chen, Stefan Sawall, Richard Sparla, Lu Su, Ursula Klingmüller, Matthias Barz, Matthias W. Hentze,* Rocío Sotillo,* and Martina U. Muckenthaler*

Cite This: *ACS Nano* 2024, 18, 11025−11041

Read Online

ACCESS | Metrics & More | Article Recommendations | Supporting Information

ABSTRACT: ALK-positive NSCLC patients demonstrate initial responses to ALK tyrosine kinase inhibitor (TKI) treatments, but eventually develop resistance, causing rapid tumor relapse and poor survival rates. Growing evidence suggests that the combination of drug and immune therapies greatly improves patient survival; however, due to the low immunogenicity of the tumors, ALK-positive patients do not respond to currently available immunotherapies. Tumor-associated macrophages (TAMs) play a crucial role in facilitating lung cancer growth by suppressing tumoricidal immune activation and absorbing chemotherapeutics. However, they can also be programmed toward a pro-inflammatory tumor suppressive phenotype, which represents a highly active area of therapy development. Iron loading of TAMs can achieve such reprogramming correlating with an improved prognosis in lung cancer patients. We previously showed that superparamagnetic iron oxide nanoparticles containing core-cross-linked polymer micelles (SPION-CCPMs) target macrophages and stimulate pro-inflammatory activation. Here, we show that SPION-CCPMs stimulate TAMs to secrete reactive nitrogen species and cytokines that exert tumoricidal activity. We further show that SPION-CCPMs reshape the immunosuppressive *Eml4-Alk* lung tumor microenvironment (TME) toward a cytotoxic profile hallmarked by the recruitment of $CD8^+$ T cells, suggesting a multifactorial benefit of SPION-CCPM application. When intratracheally instilled into lung cancer-bearing mice, SPION-CCPMs delay tumor growth and, after first line therapy with a TKI, halt the regrowth of relapsing tumors. These findings identify SPIONs-CCPMs as an adjuvant therapy, which remodels the TME, resulting in a delay in the appearance of resistant tumors.

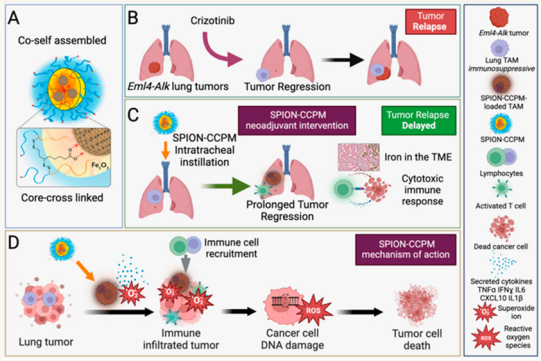

KEYWORDS: *iron homeostasis, nanoparticle, polymeric micelle, lung cancer, adjuvant therapy*

With 2.2 million new cases identified annually and approximately 1.8 million deaths registered in 2020, lung cancer is one of the most frequently diagnosed malignancies globally.[1] Lung cancer is hallmarked by the infiltration of immune cells, primarily by macrophages, called tumor-associated macrophages (TAMs). Typically, TAMs are of a tumor-promoting, alternatively activated phenotype (M2), yet can resemble other macrophage phenotypes that promote antitumor activity.[2] The extent of M2 TAM infiltration is positively correlated to poor prognosis.[3,4] M2 TAMs facilitate numerous processes that accelerate tumor growth, including nutrient delivery, angiogenesis, invasion, metastases, and suppression of antitumor immune responses, and they diminish the efficacy of anticancer therapies.[5,6] Compared to other immunologically "hot" nonsmall cell lung cancers (NSCLC), ALK-positive NSCLC harbor lower levels of tumor-infiltrating

Received: September 1, 2023
Revised: March 11, 2024
Accepted: March 15, 2024
Published: April 16, 2024

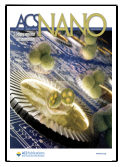

ACS Publications

© 2024 The Authors. Published by American Chemical Society

https://doi.org/10.1021/acsnano.3c08335
ACS Nano 2024, 18, 11025−11041

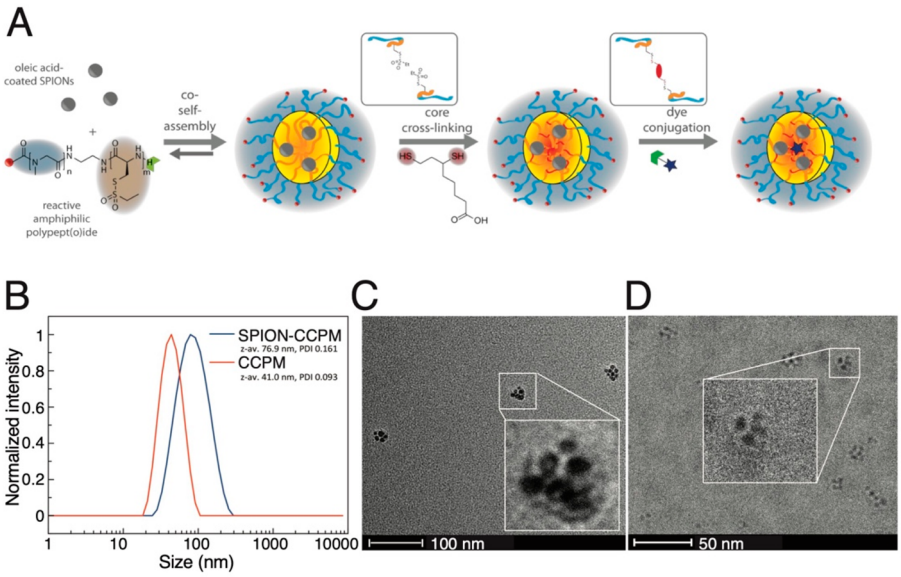

Figure 1. Synthesis and Characterization of SPION-CCPMs. (A) Synthesis of SPION-CCPMs by solution self-assembly of pSar-*block*-p(S-Cys-SO_2Et) and oleic-acid-coated SPIONs (Ocean Nanotech) followed by the addition of dihydroplipoic acid. (B) Single-angle dynamic laser light scattering data of CCPMs and SPION-CCPMs in aqueous solution at RT. (C) Representative transmission electron microscopy (TEM) image of SPION-CCPMs prepared in Milli-Q water. (D) Representative cryogenic TEM image of SPION-CCPMs in Milli-Q water.

immune cells.[7] First-line therapy in these patients consists of tyrosine kinase inhibitors (TKI), such as crizotinib, an effective approach in comparison to standard chemotherapy options.[8] However, acquired TKI resistance is inevitable and remains a critical issue. The use of immune-checkpoint inhibitors (ICI) as a monotherapy in ALK-positive tumors show modest efficacy and severe toxicities upon combination of ICI and TKI treatment.[9] Therefore, ALK-positive patients require novel approaches to completely eradicate tumors or delay relapse. Considering that the lung harbors significant basal levels of macrophage populations, therapeutic strategies that intervene by reprogramming or depleting M2 TAMs have been proposed to enhance responsiveness to current "standard-of-care" options.[10−12]

Macrophages respond to environmental signals with a broad spectrum of phenotypic changes, a process known as macrophage polarization.[13] On one end of the spectrum, pro-inflammatory macrophages secrete cytokines, such as tumor necrosis factor-alpha (TNFα), interleukin 6 (IL6), and interleukin 1 beta (IL-1β), that stimulate Th1 immune responses. In this polarization state, macrophages accumulate iron by increasing iron uptake via transferrin receptor 1 (TFR1), iron storage via ferritin light and heavy chain 1 (FtL and FtH1), and by decreasing iron export via ferroportin (FPN1).[14−16] Iron accumulation catalyzes the generation of reactive oxygen species (ROS),[17] which are required for pro-inflammatory signaling in macrophages.[18] On the other end of the spectrum, anti-inflammatory macrophages mirror the M2 TAM phenotype. Anti-inflammatory macrophages provide nutrients to surrounding cells, including iron, due to high levels of FPN1 and low levels of FtL/FtH1,[19] thus sustaining the proliferation of cancer and immune cells in the TME. Iron is essential for tumor cell survival due to its critical role in processes such as DNA synthesis, energy production, or epigenetic reprogramming.[20−22] The increased iron demand of malignant cells is satisfied mainly by increased transferrin-bound iron uptake via TFR1, a biomarker for malignancy.[23]

Tumors secrete growth factors (e.g., VEGF) to stimulate vascularization and to enhance oxygen supplies for accelerated tumor cell proliferation.[24] Inflammation in the TME contributes to rapid angiogenesis and vessel hemorrhage, causing erythrocyte extravasation into the TME and hemolysis. The rupture of erythrocytes releases heme into the TME that acts as a Damage Associated Molecular Pattern (DAMP)[25] to stimulate macrophages to adopt a pro-inflammatory phenotype.[26] Innovative approaches utilizing iron-loaded nanoparticles have allowed for the development of therapies that applies redox-active iron to target and reprogram TAMs in such a way that it resembles DAMP signaling in response to hemolytic erythrocytes.[17,26,27]

Our previous work has shown that hemolytic red blood cells induce pro-inflammatory responses in TAMs that subsequently promote tumor cell death.[27] Importantly, iron accumulation in the TME of nonsmall cell lung cancer (NSCLC) patients correlates with improved patient prognosis over time.[28] In order to selectively load macrophages with iron we developed superparamagnetic iron oxide nanoparticles loaded core-cross-linked polymeric micelles (SPION-CCPMs).[29] To ensure the efficient intracellular release of SPIONs, we employed amphiphilic polysarcosine-*block*-poly(*S*-ethylsulfonyl cysteine) copolymers[30−35] to stabilize oleic-acid-coated SPIONs in water by incorporation in the hydrophobic core of the corresponding polymeric micelles. Next, dihydrolipoic acid was used to induce core cross-linking by chemoselective disulfide formation with the *S*-ethylsulfonyl thiol groups of the polypept(o)ide and in addition oleic acid on the surface of SPIONs was replaced yielding stable SPION-CCPMs.[29] Since disulfide bonds are rapidly cleaved inside phago- or pinocytotic compartments of macrophages, SPION-CCPMs rapidly disintegrate and make SPIONs directly available inside macrophages.[29] Murine and human macrophages loaded with such SPION-CCPMs accumulate iron intracellularly and adopt a pro-inflammatory phenotype hallmarked by increased levels of TNFα, IL-6, and IL-1β, as well as increased cell surface protein levels of cluster of

https://doi.org/10.1021/acsnano.3c08335
ACS Nano 2024, 18, 11025−11041

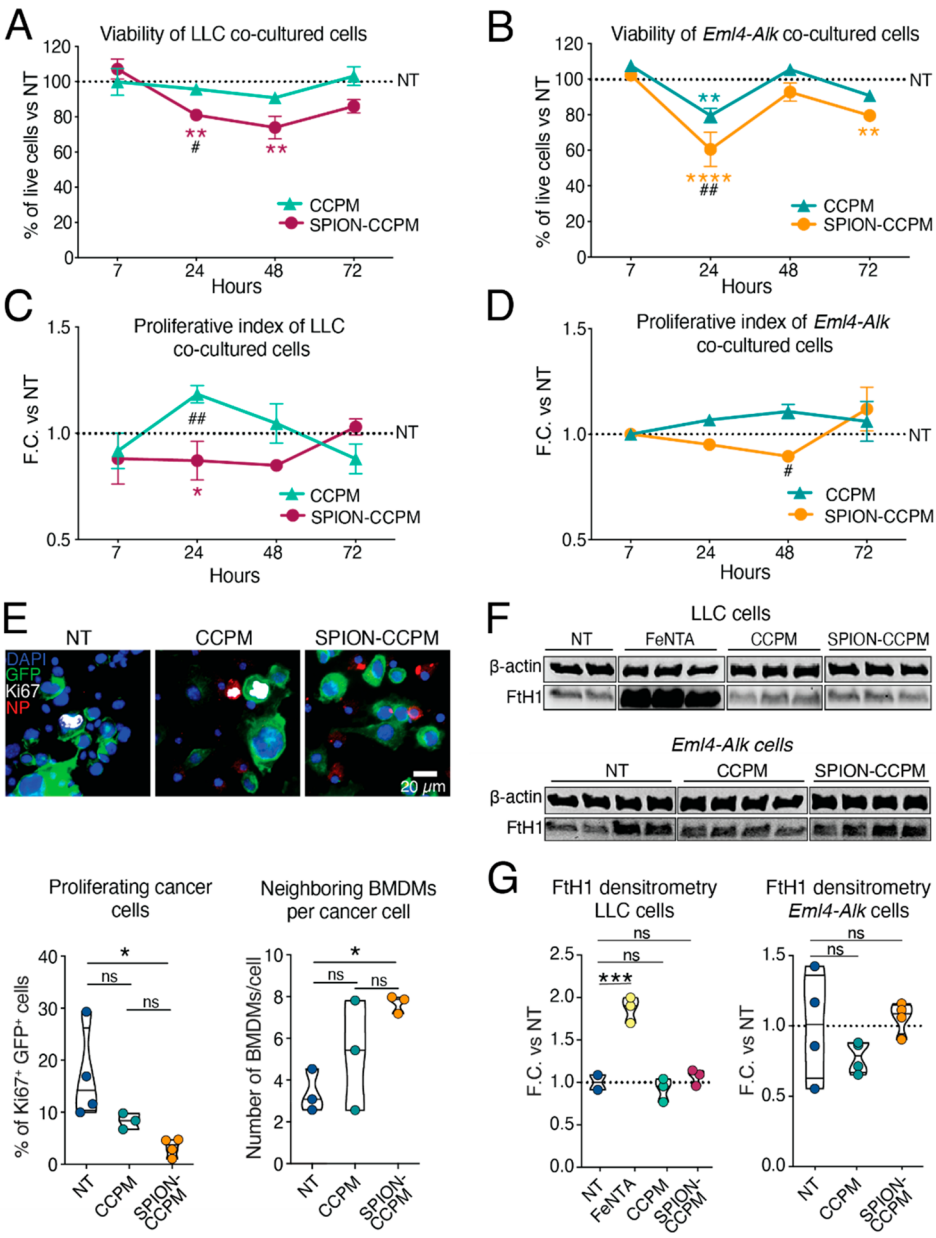

Figure 2. SPION-CCPM accumulation in macrophages reduces cancer cell proliferation in cocultures. Percentage of viable Lewis lung carcinoma (LLC) cells (A) and *Eml4-Alk* cells (B) cocultured with bone marrow-derived macrophages (BMDMs) after treatment with or without CCPMs or SPION-CCPMs. Proliferative index of LLC cells (C) and *Eml4-Alk* cells (D) maintained in coculture with BMDMs represented as a fold change (F.C.) vs nontreated (NT) cells. (E) Ki67 immunofluorescence in cocultured cells treated with or without CCPMs or SPION-CCPMs (NP) after 24 h. Cancer cells are endogenously labeled with GFP. Quantification of percentage of Ki67$^+$ cancer cells in 3000 cells obtained from three mice (below, left) and the number of neighboring BMDMs per cancer cell (below, right). (F) Western blot of the FtH1 protein in cancer cells cocultured with BMDMs treated with or without FeNTA, CCPMs, or SPION-CCPMs after 48 h. (G) Densitometry analyses of the Western blots in (F). #SPION-CCPM vs CCPM comparison; *significance of indicated colored condition vs NT condition; *$p < 0.05$, **$p < 0.005$, ***$p < 0.0005$, ****$p < 0.0001$; Two-way ANOVA (A, B, C, D, G) or one-way ANOVA (E, G). For all, at least $n = 3$.

differentiation (CD) 80, CD86, major histocompatibility complex class II (MHCII), and decreased protein levels of CD206 and MER Proto-Oncogene, Tyrosine Kinase (MerTK).[29] Of note, this response is much stronger than the one observed against plain SPIONs or feraheme and has set standards in our laboratories for macrophage repolarization.[29]

Here, we show that SPION-CCPMs ingested by bone marrow-derived macrophages (BMDMs) efficiently reduce the proliferation of cocultured lung cancer cells. We further demonstrate that SPION-CCPM-loaded macrophages initiate pro-inflammatory responses that induce oxidative stress and DNA damage in neighboring cancer cells. In mice, SPION-CCPMs reprogram the TME and stimulate the recruitment of cytotoxic T cells (CD8$^+$). As a consequence, the tumor growth is reduced. Most impressively, when SPION-CCPMs are administered to *Eml4-Alk* tumor-bearing mice as an adjuvant following treatment with a tyrosine kinase inhibitor, tumor growth is curtailed upon tumor regrowth, suggesting that SPION-CCPM treatment may maintain the benefit of ALK inhibition in the clinic.

https://doi.org/10.1021/acsnano.3c08335
ACS Nano 2024, 18, 11025−11041

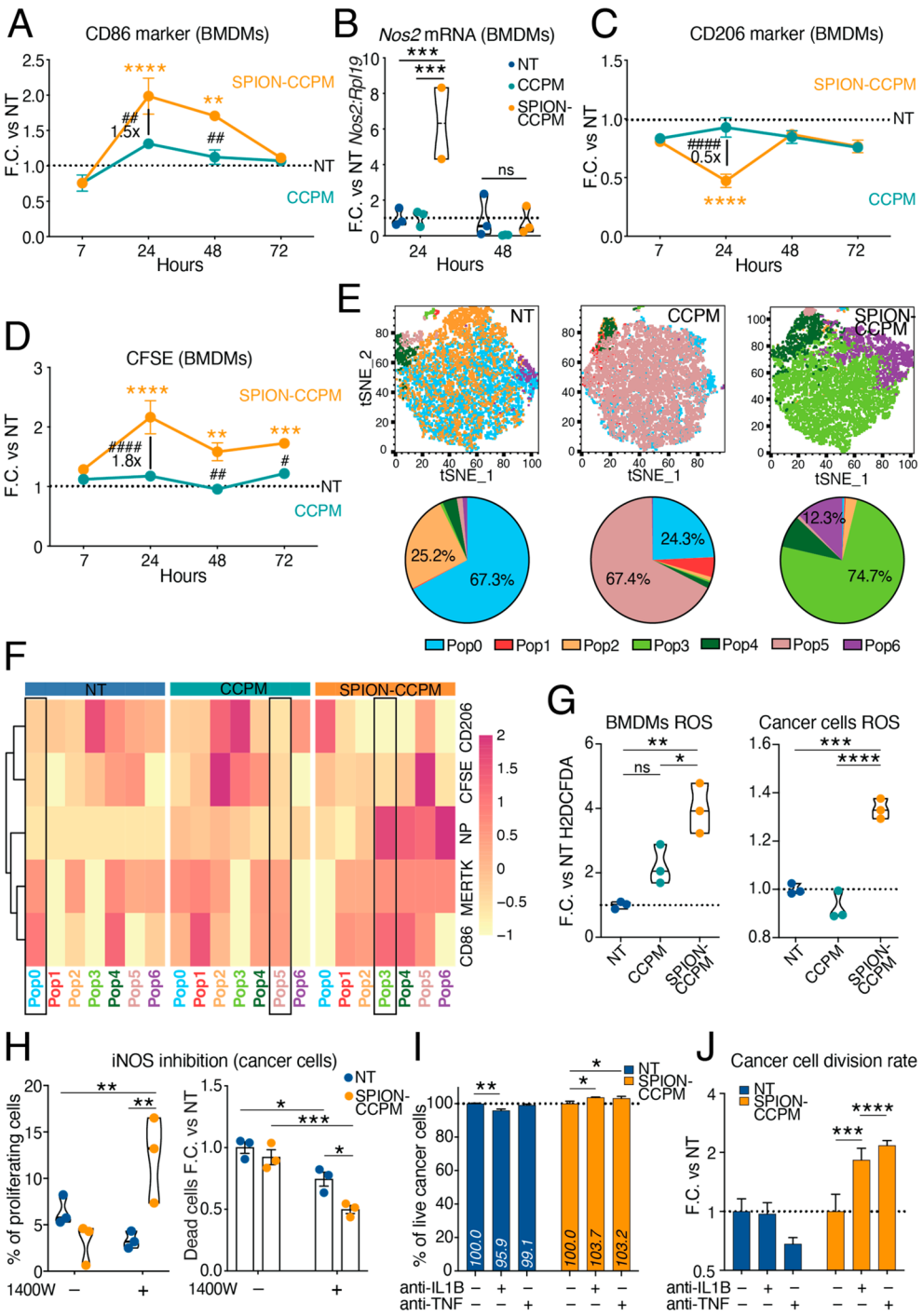

Figure 3. SPION-CCPM-loaded macrophages phagocytose cancer cells and secrete factors that reduce proliferation and viability of cocultured cancer cells. CD86 cell surface levels (A), *Nos2* mRNA levels (B), CD206 cell surface levels (C), or cancer cell internalization (CFSE signal) over time (D) in bone marrow-derived macrophages (BMDMs) cocultured with LLC cancer cells. (E) Distribution (up, tSNE plots) and frequency (down, pie charts) of clustered CD45$^+$ populations. (F) Cluster analysis heatmap of marker frequency in cocultured macrophages. Data scaled by row. The most abundant population in each condition is highlighted. (G) Reactive oxygen species (ROS) measurement in cocultured BMDMs (left) and LLC cells (right) after 24 h. (H) Percentage of proliferating cells (left) and viable cocultured cancer cells (right) after 48 h inhibition of iNOS with 1400 W. (I) Percentage of live cancer cells after 24 h and (J) cancer cell division rate after 72 h of coculture with BMDMs and neutralization of IL-1β or TNF. (A, B, C, D, G, H, J). Values represented as fold change (F.C.) vs the nontreated (NT) condition. #SPION-CCPM vs CCPM; *significance of colored condition vs NT condition; *$p < 0.05$, **$p < 0.005$, ***$p < 0.0005$, ****$p < 0.0001$; Two-way ANOVA (A, B, C, D, H, I, J) or one-way ANOVA (G). For all, $n = 3$.

RESULTS

Synthesis and Characterization of SPION-CCPMs. SPION-CCPMs were synthesized as previously described[29] (Figure 1A). Briefly, core cross-linked polymeric micelles (CCPMs) were constructed by first synthesizing block copolymers of polysarcosine and poly(*S*-ethylsulfonyl-L-cysteine). Then, oleic-acid-coated SPIONs (γ-maghemite Fe_2O_2, D = 6 nm) were solubilized using copolymers and dihydrolipoic

https://doi.org/10.1021/acsnano.3c08335
ACS Nano 2024, 18, 11025−11041

acid, which in addition cross-linked the CCPMs and exchanged the oleic acid on the SPION surface.[29] This process yielded SPION-CCPMs with a hydrodynamic diameter of 77 nm (Figure 1B) and an iron content of 33 wt% . Empty CCPMs were prepared from block copolymers according to previous reports[31] with a hydrodynamic diameter of 41 nm in aqueous solution. The internal structure of SPION-CCPMs was assessed by conventional and cryogenic transmission electron microscopy (cryo-TEM). With both technologies, the SPIONs were localized in the center of the particles and surrounded by a polymer matrix, which was directly visible in conventional TEM (Figure 1C). In cryoTEM, the difference in scattering contrast limited the visualization of the CCPMs next to the SPION-containing core (Figure 1D). In all cases, the SPION-CCPMs contained multiple SPIONs of around 6 nm in diameter. In line with our former observations, SPION-CCPMs degraded at elevated glutathione levels of 10 mM and released iron, which can modulate macrophage activity.

SPION-CCPM-Loaded Macrophages Reduce Cancer Cell Viability and Proliferation in Cocultures. Based on our previous discovery that SPION-CCPM-treated macrophages adopt a pro-inflammatory phenotype,[29] we now aimed to investigate whether they exert tumoricidal activity against lung cancer cells. We cocultured BMDMs with Lewis lung carcinoma (LLC; C57Bl/6 genetic background) or *Eml4-Alk* mouse-derived (FVB genetic background) lung cancer cells and treated with SPION-CCPMs, CCPMs (nanoparticle shell as control), or left untreated (NT). SPION-CCPMs and nonloaded CCPMs were predominantly taken up by macrophages in both cocultures (Supplemental Figure 1A,B). Interestingly, SPION-CCPM treatment reduced cancer cell viability by ∼1.5-fold at 48 h in LLC/BMDM and ∼2-fold at 24 h in *Eml4-Alk*/BMDM cocultures (Figure 2A,B). These findings were consistent with a reduced proliferation index at 24 and 48 h for both LLC and *Eml4-Alk* cells, respectively (Figure 2C,D), and a marked reduction in the proliferation marker Ki67[36] in SPION-CCPM-treated cocultures (Figure 2E, left). Interestingly, we found that SPION-CCPM-loaded macrophages were closer in proximity to cancer cells than those from CCPM or NT cocultures (Figure 2E, right).

Importantly, we found no increase in the levels of the iron storage protein FtH1 in LLC and *Eml4-Alk* cancer cells treated with SPION-CCPMs, in contrast to treatment with the iron source ferric nitrilotriacetate (FeNTA), suggesting that SPION-CCPMs do not serve as a source of iron for cancer cells (Figure 2F,G).

To understand how SPION-CCPM-treated macrophages alter cellular processes in lung cancer cells, we examined the cancer cell proteomes by data-dependent mass spectrometric analysis and detected around 3800 proteins (Supplemental Figure 1C,D). In SPION-CCPM-treated cocultured lung cancer cells, the levels of proteins related to UV response, the unfolded protein response, and the G2M checkpoint were increased (Supplemental Figure 1E), whereas proteins involved in cell proliferation or viability pathways, such as MTORC1 and mitotic spindle, showed decreased levels compared to NT cultures. Consistent with an enrichment in the UV-induced DNA damage pathway, we saw an increase in the number of γ-H2AX^{+} foci per cancer cell (Supplemental Figure 1F, bottom left), which is known to increase upon formation of double-stranded DNA breaks caused by excessive oxidant radicals.[22,37] In line with this, mRNA levels of the NRF2 target gene *Nqo1* were increased, and those of the glutathione-producing enzyme *Gclc* were reduced upon SPION-CCPM, but not upon treatment with the nanoparticle shell CCPM (Supplemental Figure 1G,H). Additionally, total intracellular glutathione (GSH) levels were reduced 2-fold in SPION-CCPM-treated cocultures, akin to treatment with the pan-HDAC inhibitor suberoylanilide hydroxamic acid (SAHA; positive control;[38] Supplemental Figure 1I). This result suggests that cancer cells experience oxidative stress in response to SPION-CCPM internalization by macrophages and that such oxidative stress may lead to DNA double-strand breaks. Consistently, SPION-CCPM-loaded macrophages were frequently observed to be in close proximity to DNA-damaged cancer cell nuclei (Supplemental Figure 1F, bottom right), suggesting that SPION-CCPM-stimulated macrophages secrete factors in a paracrine manner that induce oxidative or cytotoxic stress in cancer cells. Taken together, we propose that SPION-CCPM uptake by macrophages and consequent iron loading induce oxidative stress and DNA damage in neighboring cancer cells, resulting in cell cycle arrest and reduced cell proliferation.

SPION-CCPM Uptake in Cocultured Macrophages Induces an Acute Inflammatory Response and Increased Phagocytic Activity. We next focused on phenotypic changes that occur in the macrophages. Similar to SPION-CCPM-treated macrophage cultures,[29] BMDMs in SPION-CCPM-treated cocultures transiently expressed pro-inflammatory markers, such as elevated CD86 and *Nos2* levels (Figure 3A,B) and decreased expression of the anti-inflammatory marker CD206 (Figure 3C). To evaluate the phagocytic activity of macrophages, cancer cells were stained with carboxyfluorescein succinimidyl ester (CFSE) prior to adding BMDMs. Interestingly, the CFSE fluorescence signal was detected at higher levels in SPION-CCPM-treated, compared to CCPM or NT macrophages (Figure 3D), suggesting that SPION-CCPM treatment may have stimulated macrophages to phagocytose cancer cells. Alternatively, cancer cells may become damaged by the proximity of SPION-CCPM-treated macrophages, as suggested by the results from Figure 1, and thus, increased cancer cell debris is then phagocytosed by macrophages. Cluster analysis was performed based on the expression of the cell surface markers CD86, CD206, and MerTK (a macrophage receptor mediating the phagocytic clearing of apoptotic bodies in a process called efferocytosis),[39] along with NP fluorescence signal intensity and the cancer cell label CSFE 24 h after coculturing. We found that macrophages could be classified into 6 subpopulations that differed significantly between SPION-CCPM, CCPM, and control (NT) treatments (Figure 3E,F). A total of 74.7% of SPION-CCPM-treated BMDMs were hallmarked by NP^{high}, CD86^{high}, MerTK^{med}, and CD206^{neg} (Pop3; green), whereas in the NT and CCPM cultures, the largest populations of macrophages were characterized by a mix of CD86^{med}, MerTK^{med}, and CD206^{med} (Pop0 and Pop5; blue and mauve, respectively), demonstrating the strong effect of SPION-CCPMs to polarize the majority of macrophages to a pro-inflammatory phenotype. In addition, CFSE was detectable in macrophage subpopulations in response to SPION (13.05%) and to a lesser extent following CCPM (8.13%; Figure 3D).

Secreted Factors from SPION-CCPM-Loaded Macrophages Reduce Cancer Viability. SPION-CCPM-loaded macrophages were found in the vicinity of cancer cells. To investigate whether physical contact between SPION-CCPM-treated macrophages and cancer cells is required to reduce the viability of cancer cells, we established a trans-well culture system. Cancer cell viability was reduced upon SPION-CCPM

https://doi.org/10.1021/acsnano.3c08335
ACS Nano 2024, 18, 11025−11041

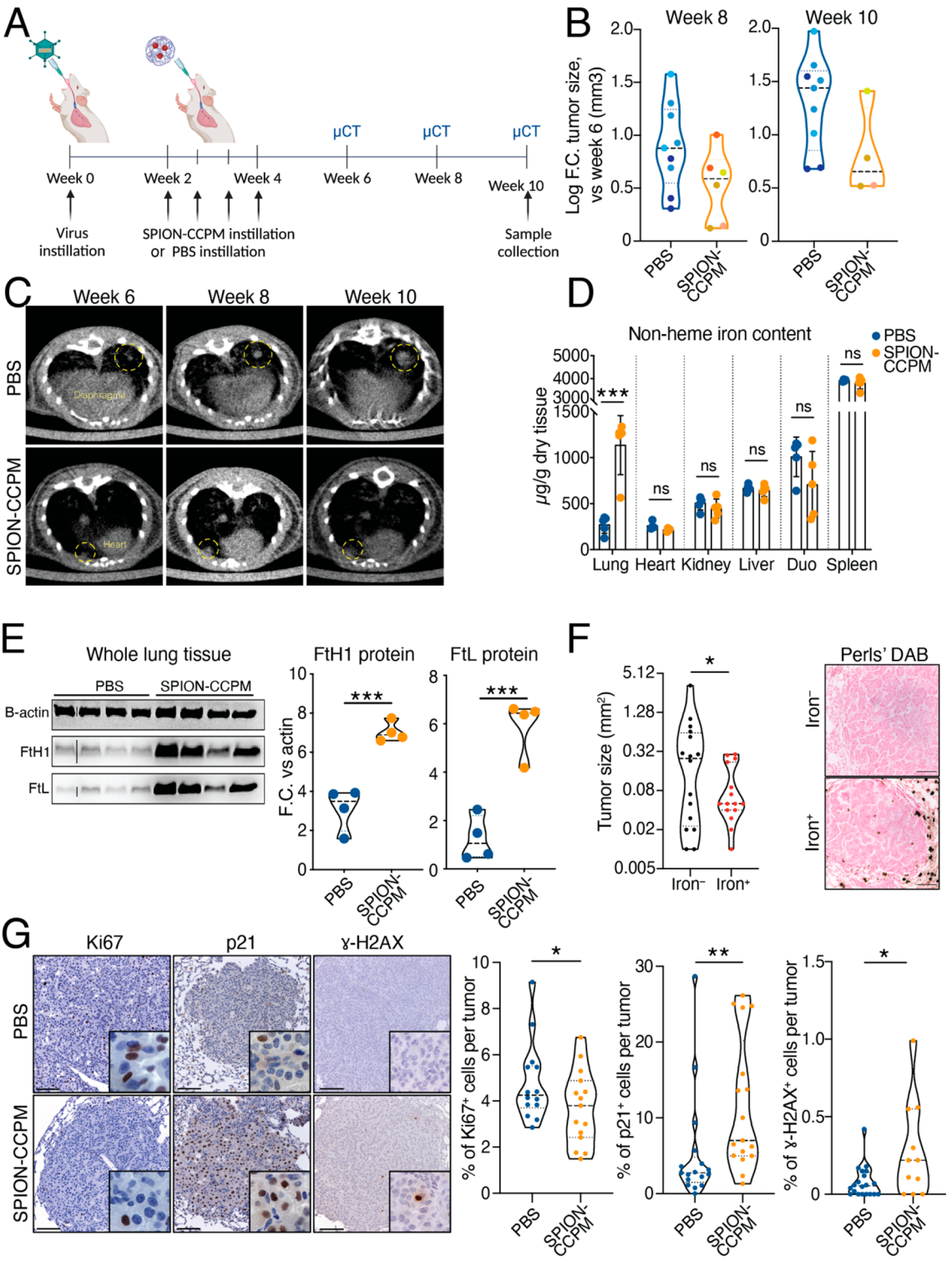

Figure 4. SPION-CCPM instillation induces DNA damage and reduces tumor growth in mice. (A) Experimental design. (B) Tumor size at weeks 8 and 10 analyzed by μCT; data shown as log fold-change (Log F.C.) compared to week 6 (first time point measurable after viral clearance). Each dot represents a tumor which are colored according to each mouse. We applied a linear mixed model with random intercept for "animal" to account for the fact that multiple tumors were evaluated per animal. (C) Representative μCT lung images from PBS and SPION-CCPM-treated mice at weeks 6, 8 and 10; yellow circles indicate a growing tumor. (D) Nonheme iron content in organs. (E) Ferritin heavy chain 1 (FtH1), ferritin light chain (FTL) and β-actin protein detection by Western blot (left). Protein levels were quantified (right) by comparing signal protein intensity against β-actin levels and represented as F.C. (F) Size of iron$^-$ and iron$^+$ tumors. Right, representative images of Perls' Prussian Blue DAB staining. (G) Ki67, p21 and γ-H2AX representative tumor images (left) from PBS and SPION-CCPM-instilled tumor-bearing mice. Quantification of positive cells per tumor (right). (F, G) Scale bar 100 μm. Each dot represents a tumor (B, F, G) or a mouse (D, E). *$p < 0.05$, or unpaired t test (D−G). $n = 5$ mice per group except B, ($n = 3$ PBS; $n = 4$ SPION-CCPM) and D, E ($n = 4$).

https://doi.org/10.1021/acsnano.3c08335
ACS Nano 2024, 18, 11025−11041

treatment in the trans-well culture to similar levels as those in the coculture setting (Supplemental Figure 2A), suggesting that macrophage-secreted factors mediate the response to SPION-CCPM treatment.

Activated macrophages secrete ROS and reactive nitrogen species (RNS) upon iron accumulation.[40] Flow cytometry analysis of oxidized H2DCFDA fluorescent probes showed that SPION-CCPM treatment increased ROS levels in cocultured macrophages as well as in cancer cells compared to CCPM-treated or NT (Figure 3G). We next aimed to determine the mode of cell death imposed on cancer cells when experiencing neighboring SPION-CCPM-treated macrophages. We showed that increased ROS levels in cancer cells did not induce detectable lipid peroxidation or decreased mRNA expression of *Gpx4* in cancer cells, but interestingly, reduced cancer cell viability was counteracted by the ferroptosis inhibitor liproxstatin, as determined by LDH release. This suggests that ferroptosis may influence[41] cancer cell death triggered by SPION-CCPM-loaded macrophages (Supplemental Figure 2B−D). Furthermore, inhibition of necrotic, apoptotic, or autophagic cell pathways through the use of necrostatin, Q-VD-OPh (QVD), and 3-methyladenine (3MA), respectively, showed that SPION-CCPM treatment additionally induced cell death through pathways that are inhibited by QVD and 3MA (Supplemental Figure 2E).

Reactive nitrogen species (RNS) are produced in macrophages by the enzyme iNOS (*Nos2*)[42] and can be repressed by the iNOS inhibitor, 1400W, which then depletes nitric oxide (NO) levels.[43] We, therefore, tested whether the inhibition of iNOS, which was upregulated in SPION-CCPM-loaded macrophages (Figure 3B), could increase cancer cell viability. Pharmacological inhibition of iNOS increased cancer cell proliferation and reduced the number of dead cells in SPION-CCPM cocultures (Figure 3H), but did not modify the expression of CD206 and CD86 in macrophages (Supplemental Figure 2F), suggesting that secreted RNS contribute to the observed reduction in cancer cell proliferation and viability.

Next, we analyzed whether the secretion of pro-inflammatory cytokines, such as IL-1β and TNF, by SPION-CCPM-loaded macrophages,[29] contributes to the reduced cancer cell viability. We applied neutralizing antibodies for IL-1β or TNFα and showed that the number of viable cancer cells in SPION-CCPM-treated cocultures increased at 24 h (Figure 3I) and the rate of cancer cell division approximately doubled at 72 h (Figure 3J). Macrophages incurred an upregulation of CD206 levels upon TNFα neutralization, yet CD86 levels remained relatively unaffected by IL-1β or TNFα neutralization (Supplemental Figure 2G), suggesting that macrophage pro-inflammatory polarization was unaffected upon cytokine neutralization. Taken together, our data suggest that SPION-CCPMs induce ROS/RNS as well as cytokine production in macrophages that impair cancer cell function multifactorially and activate cancer cell death. Mass spectrometric analysis of SPION-CCPM-treated macrophages' proteome detected approximately 4000 proteins and revealed enrichment in a wide range of inflammatory pathways involved in adaptive immune responses, antigen processing-cross presentation, and detoxification of ROS (Supplemental Figure 2H−J), suggesting that additional factors secreted from macrophages may contribute to cancer cell death.

SPION-CCPMs are Taken up by Innate Immune Cells of the Lung and Stimulate Pro-Inflammatory Responses. To analyze whether the SPION-CCPM effects observed in BMDMs can also be elicited in the mouse lung, an organ highly populated with macrophages, we intratracheally administered SPION-CCPMs in healthy mice to determine the longevity and potency of the inflammatory response. The immune cell composition was analyzed in the bronchoalveolar lavage (BAL) in a time course manner (Supplemental Figure 3A) by flow cytometry. The SPION-CCPM signal first appeared in interstitial macrophages (IM; CD11b$^+$ CD64$^+$) after 4 h, consistent with previous observations.[29] At 24 h, the SPION-CCPM signal was additionally detected in neutrophils (CD11b$^+$ Ly6G$^+$), eosinophils (CD11b+ SiglecF$^+$), and alveolar macrophages (AM; CD11c$^+$ SiglecF$^+$; Supplemental Figure 3B). 48 h post-treatment, the SPION-CCPM signal was mainly detected in dendritic cells (DC; CD11c$^+$and MHCII^{high}). 24 h after SPION-CCPM instillation, we observed a pronounced increase in mRNA expression of inflammatory cytokines (*Il6* and *Il1b*) and an oxidative response gene (*Hmox1*; Supplemental Figure 3C), correlating with the increase in nonheme iron content in lung tissue (Supplemental Figure 3D). SPION-CCPM instillation in the lung did not significantly alter serum iron levels (Supplemental Figure 3E), suggesting that the iron contained in SPION-CCPMs is gradually absorbed into lung tissue and is not significantly distributed systemically. Our data demonstrate that SPION-CCPMs instilled into the lung are taken up by innate immune cells, where they induce a widespread yet transient pro-inflammatory activation.

Pulmonary SPION-CCPM Instillation Diminishes Lung Tumor Growth. We next tested whether SPION-CCPM instillation reduced cancer growth in a murine lung adenocarcinoma (LUAD) model. *Eml4-Alk* tumors were established by intratracheal instillation of an adenovirus containing a CRISPR-Cas9 construct that generates an endogenous *Eml4-Alk* rearrangement leading to LUAD.[44] Two weeks after virus instillation, SPION-CCPMs or PBS were intratracheally instilled every 4 days for a total of four administrations (Figure 4A). After 6 weeks, tumor sizes were measured by microcomputed tomography (μCT) and we followed tumor growth every 2 weeks by continued imaging. Consistent with the results obtained in the coculture experiments, SPION-CCPM-administered mice showed a notable trend toward a diminished tumor growth rate compared to control mice (Figure 4B,C). We observe that the median of the PBS group increases from 0.895 to 1.305 while the median of the SPION groups varies between 0.523 and 0.809. Similar to healthy mice (Supplemental Figure 3D), SPION-CCPM treatment increased the nonheme iron content of the lung (Figure 4D) and increased expression of the iron storage proteins FtL and FtH1 (Figure 4E). However, iron released from SPION-CCPMs was largely confined to nontumor tissue areas (Figure 4F) and remained within tumor-bearing lungs, as other organs (e.g., liver, spleen, or duodenum) displayed unaltered iron content (Figure 4D).

We previously showed that iron accumulation in the TME of human nonsmall cell lung cancer (NSCLC) is associated with a smaller tumor size compared to tumors devoid of iron.[27,28] To validate these findings in *Eml4-Alk* tumors, we stratified tumors into iron$^+$ or iron$^-$ by denoting the presence of iron-loaded cells within the immediate tumor periphery and inside the tumor boundary. In SPION-CCPM-treated mice, we found that iron$^+$ tumors were smaller than iron$^-$ tumors (Figure 4F), consistent with our results from human NSCLC.[45] In addition, in SPION-CCPM-treated tumors, the number of Ki67$^+$ nuclei was reduced, the number of p21$^+$ nuclei was increased, and more γ-H2AX$^+$

https://doi.org/10.1021/acsnano.3c08335
ACS Nano 2024, 18, 11025−11041

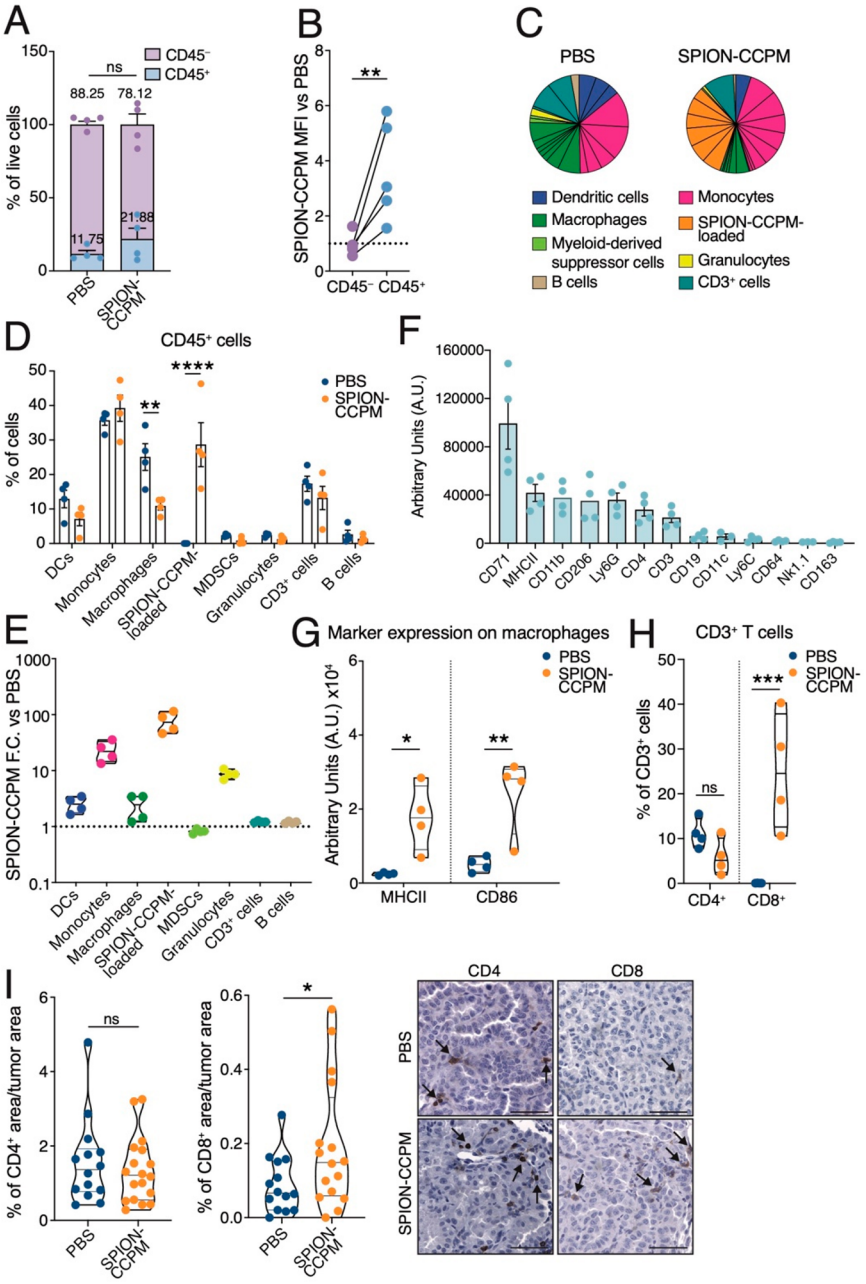

Figure 5. SPION-CCPMs alter the tumor microenvironment toward a more pro-inflammatory and cytotoxic immune landscape. (A) Flow cytometry measurement of CD45⁺ immune cells and CD45⁻ nonimmune cells from the lungs of PBS or SPION-CCPM-treated *Eml4-Alk* mice. (B) Quantification of SPION-CCPM median fluorescence intensity (MFI) in CD45⁺ and CD45⁻ lung cells by flow cytometry. (C) Representation of immune cell types organized by ontological marker groupings; chart indicative of all mice. (D) Quantification of the frequencies of CD45⁺ immune cell types represented by biological replicate. (E) SPION-CCPM fluorescence signal intensity (MFI) in immune cells of SPION-CCPM-treated mice. (F) Relative cell surface marker levels on SPION-CCPM-loaded immune cells (orange group) ranked highest to lowest. (G) Expression levels of the indicated markers in macrophages. (H) Percentage of CD4⁺ and CD8⁺ T cell populations measured by flow cytometry. (I) Percentage of CD4⁺ (left) or CD8⁺ (right) area per tumor area. Each dot represents a tumor. Representative images are shown. Arrows indicate positive cells. Scale bar 50 μm. *$p < 0.05$, **$p < 0.005$, ***$p < 0.0005$, ****$p < 0.0001$, unpaired *t*-test (A, B, I) or two-way ANOVA (D, G, H). In all, $n = 4$ mice per group.

cells were detected compared to PBS mice (Figure 4G), suggesting that tumor proliferation is attenuated, a proportion of tumor cells undergo cell cycle arrest, and that SPION-CCPM treatment induces DNA damage.

SPION-CCPMs Reprogram the Tumor-Associated Immune Landscape by Inducing Pro-Inflammatory and Cytotoxic Immune Cells. We next aimed to understand the effect of SPION-CCPM treatment on the tumor immune compartment. Increased *Nos2* and *Tnf* mRNA levels were found in SPION-CCPM-treated samples (Supplemental Figure 4A), suggesting immune cell activation. We analyzed the composition of CD45⁺ immune cells by flow cytometry. In SPION-CCPM-treated mice, we found a slight enrichment of CD45⁺ immune cells compared to that in PBS mice (Figure 5A). CD45⁺ cells showed a more pronounced SPION-CCPM signal intensity than CD45⁻ cells (Figure 5B) even though the percentage of

https://doi.org/10.1021/acsnano.3c08335
ACS Nano 2024, 18, 11025−11041

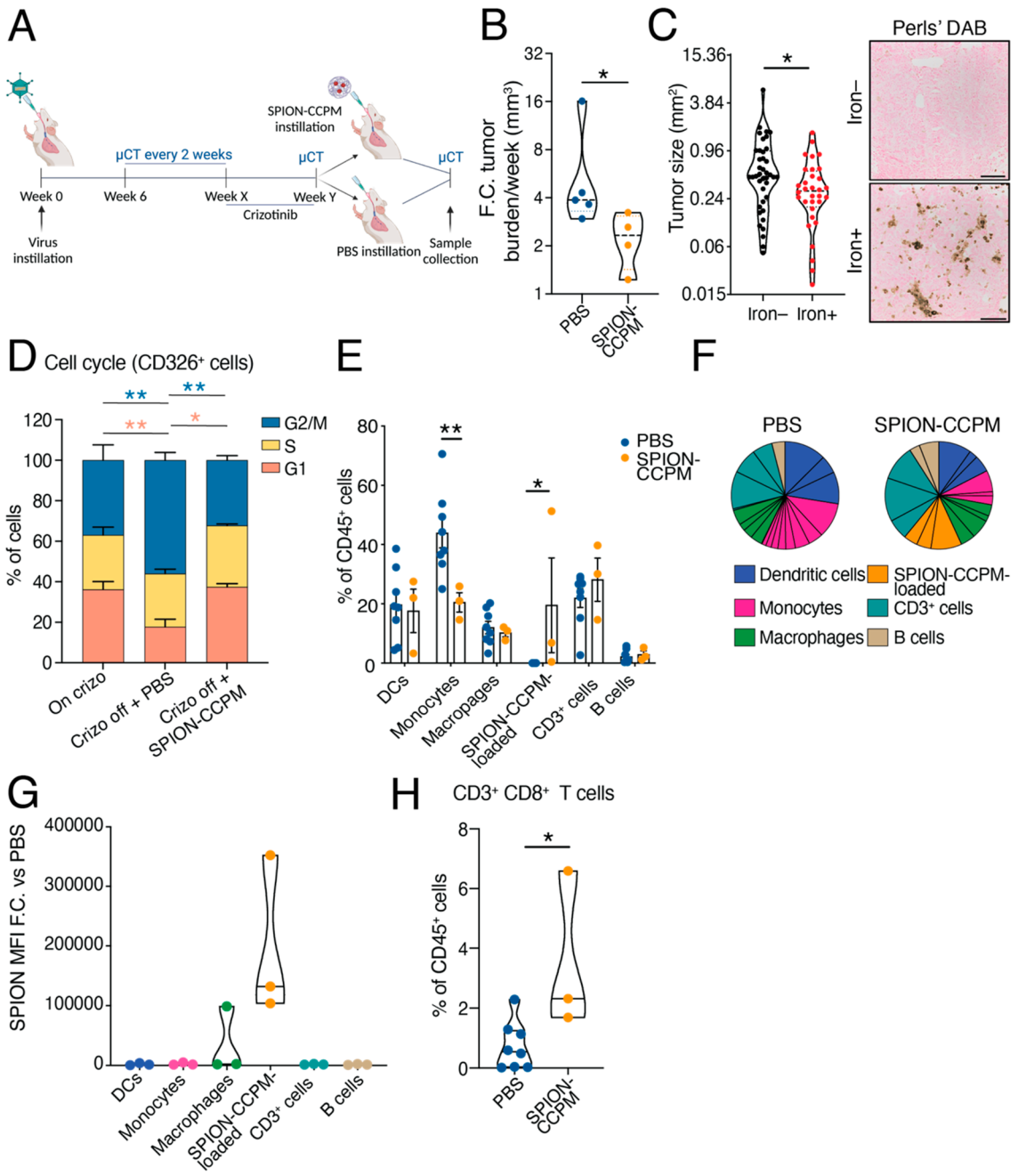

Figure 6. SPION-CCPM treatment following crizotinib delays tumor regrowth in mice. (A) Experimental design. (B) Fold-change (F.C.) of tumor burden per week after PBS or SPION-CCPM treatment measured by μCT (left). Each dot represents a mouse. (C) Tumor size of iron⁺ and iron⁻ tumors; each dot represents a tumor. DAB enhanced Perls' Prussian Blue staining in tumor tissue (right). Scale bar 100 μm. (D) Cell cycle analysis of CD326⁺ cells represented as percentage of cells in each cell cycle phase. (E) Frequency of immune cell groups out of the CD45⁺ population. (F) Representation of the frequency of immune cell groups after cluster analysis of cell surface markers using the Phenograph algorithm (FlowJo); charts indicative of all mice. (G) SPION-CCPM fluorescence signal intensity (MFI) in immune cell groups of SPION-CCPM mice. (H) Percentage of CD3⁺CD8⁺ T cells. *$p < 0.05$, **$p < 0.005$, Mann−Whitney test (B, C), two-way ANOVA (D, E), or unpaired *t*-test (H). PBS (n = 8 mice, except B, n = 5) and SPION-CCPM (n = 3 mice, except B and C, n = 4).

SPION-CCPM-positive cells was similar in CD45⁺ and CD45⁻ cells (Supplemental Figure 4B), suggesting immune cells accumulate higher levels of SPION-CCPMs than nonimmune cells. K-means clustering of CD45⁺ lung cells revealed 26 distinct cell types (clusters) in SPION-CCPM-treated mice compared to 22 clusters in PBS-treated control mice, suggesting that the heterogeneity of immune cell types increases in response to SPION-CCPM treatment (Figure 5C and Supplemental Figure 4C). Clusters were grouped according to marker similarity and showed that mice treated with SPION-CCPMs had reduced numbers of macrophages compared with PBS mice (Figure 5D). The SPION-CCPM-loaded group (orange) contained the brightest SPION-CCPM signal intensity, followed by monocytes (magenta), granulocytes (yellow), dendritic cells (DCs) (blue), and macrophages (green) (Figure 5E), and it occupied a considerable distinct portion of the immune landscape (approximately 30% of CD45⁺ cells). Strikingly, the SPION-CCPM-loaded cells were incom-

https://doi.org/10.1021/acsnano.3c08335
ACS Nano 2024, 18, 11025−11041

parable ontologically to immune cells found in PBS mice (Supplemental Figure 4C) and were hallmarked by unusually mixed immune cell type markers, making their characterization into conventional immune cell groupings challenging. These markers included myeloid cell markers (CD11b, MHCII, and Ly6G), lymphocytic cell markers (CD3, CD4, and CD19), and activation markers (CD206; Figure 5F). Polarization markers evaluated on macrophages showed increased MHCII and CD86 levels upon SPION-CCPM treatment (Figure 5G), suggesting pro-inflammatory activation. These markers were found to be unchanged in DCs, monocytes, and granulocytes (data not shown). Evaluation of T cells showed an increase in $CD8^+$ cytotoxic T cell frequency (Figure 5H,I), suggesting that SPION-CCPM treatment stimulates antitumor activity through the enrichment of cytotoxic $CD8^+$ T cell population. Altogether, these results unveil that SPION-CCPMs have widespread *in vivo* effects inducing an antitumor environment which decreases TAMs and increases a cytotoxic and pro-inflammatory TME.

SPION-CCPM Adjuvant Therapy Effectively Reduces Cancer Regrowth. The development of resistance to targeted therapies in ALK-positive patients remains a major challenge, and combining TKI with immunotherapy has not shown significant clinical benefits.[9] Considering the immune modulatory effect of SPION-CCPMs we assessed whether macrophage priming with SPION-CCPM instillation in tumor-bearing mice shows promise as an adjuvant therapy. *Eml4-Alk* tumors were monitored by μCT, grown to 30 mm^3 volume, and then treated with crizotinib (TKI targeting ALK)[46] until tumors regressed or mice became noncompliant. Subsequently, PBS or SPION-CCPMs were administered twice, and tumor regrowth was monitored by μCT (Figure 6A). We found that tumors rebounded significantly more slowly with SPION-CCPM adjuvant therapy (Figure 6B). Additionally, DAB-enhanced Perls' staining showed that tumors surrounded by iron-enriched immune cells were smaller than $iron^-$ tumors and that $iron^+$ cells were recruited into the tumor parenchyma (Figure 6C). Crizotinib has been described to induce G1/S arrest.[47] Analysis of the DNA content of epithelial cells ($CD326^+$) showed that SPION-CCPM treatment sustained crizotinib-induced G1 arrest in comparison to PBS mice (Figure 6D). This finding suggests that SPION-CCPMs slow tumor cell growth and, therefore, contribute to bolstering the cell cycle arrest effects of crizotinib.

In contrast to our previous monotherapy experiment (Figure 4), the number of monocytes was reduced in SPION-CCPM-treated mice (Figure 6E,F), suggesting that SPION-CCPMs as an adjuvant therapy reduce monocyte lung recruitment. Similar to the monotherapy experiment, we found SPION-CCPM signal intensity primarily in the SPION-CCPM-loaded group (orange) and macrophage group (green) (Figure 6G). Additionally, we found a higher percentage of cytotoxic T cells ($CD8^+$ T cells) present in SPION-CCPM-treated mice compared to PBS-treated control mice (Figure 6H), further corroborating the SPION-CCPM-induced cytotoxic and pro-inflammatory TME, which likely contributes to reduced tumor growth.

DISCUSSION

Lung tumors seize innate immune cells which then support cancer cell expansion and interfere with the effectiveness of anticancer therapies.[4,6] The targeting of macrophages by immunotherapy is now included as a standardized treatment of multiple cancer entities, including NSCLC, where an improvement in prognosis and survival has been observed.[48] Lung cancer therapies are frequently hampered by ineffective drug delivery, imprecise drug targeting, and unwanted side effects. Nanoscale formulations can circumvent some of these challenges by improving the targeting of medication.

The first important finding of this study was that SPION-CCPM-treated macrophages impair the viability of LLC and *Eml4-Alk* tumor cells in a coculture model. The observed effect was caused by the iron payload as the treatment with the nanoparticle shell alone (CCPM) did not exert similar responses. This finding extends previous data showing that iron accumulation in macrophages triggers a phenotypic switch to a pro-inflammatory state that exerts antitumor activity and reduces tumor growth.[27,49]

We further demonstrated that cancer cells near SPION-CCPM-loaded macrophages showed increased levels of oxidative stress markers, DNA damage, and reduced proliferation. The reduction of cancer cell viability was caused by secreted factors from SPION-CCPM-containing macrophages, including RNS and cytokines (IL-1β, TNFα). These findings may explain previous data where M1/pro-inflammatory macrophage polarization (stimulated by LPS and IFNγ) sensitizes A549 lung cells to cisplatin and induce senescence and apoptosis via secreted factors.[50] Further work is needed to detail more precisely how additional secreted factors produced by iron-loaded macrophages contribute to inducing oxidative stress in cancer cells and reducing their viability. To overcome the limitations of single factor analyses in cultured cells, simultaneous proteomic, transcriptomic, and metabolomic analysis needs to be applied in a time-resolved manner together with modeling and computational approaches to elucidate the complex dynamics of the communication between cancer cells and a broad spectrum of macrophage phenotypes present in the TME.[51−53] Nevertheless, our data support the concept that iron accumulation in macrophages (e.g., in response to hemolytic red blood cells)[15,27] or iron-containing nanoparticles damage neighboring cells in a paracrine manner via ROS induction.

ROS induction (e.g., by chemotherapeutics or radiotherapy) has long been considered to hit an Achilles heel of tumor cells as they were assumed to be less resilient than surrounding tissue. Pronounced dose limiting toxicity and limited success in clinical trials suggests that systemic treatment with redox targeting drugs is challenging.[54−56] We propose that the combination of systemic ROS-inducing therapies and SPION-CCPM-loaded macrophages would allow local increase of ROS to tumoricidal levels as TAMs home in on cancer cells. Consistent with this hypothesis, a second important result of this study is that *Eml4-Alk* cancer cells persisting after crizotinib treatment are more responsive to iron-loaded macrophages. This result may be explained by the finding that crizotinib treatment in addition to ALK and cMET inhibition, also increases superoxide production.[57] Our data show that crizotinib-regressed tumors in an *Eml4-Alk*-driven lung cancer mouse model harbored DNA damage and a reduced growth rate caused by SPION-CCPM treatment. This provides an emerging therapeutic strategy for patients with limited therapeutic options, positioning SPION-CCPMs as a highly promising adjuvant agent. Patient stratification by a recently defined set of biomarkers that predict susceptibility to redox drugs in lung cancer may further improve the efficacy of SPION treatment in patients.[58]

Several anticancer strategies capitalize on targeting molecular signaling pathways to inhibit the recruitment of myeloid cells (i.e., CCL2 inhibitors; in clinical trial NCT00537368).[59,60]

https://doi.org/10.1021/acsnano.3c08335
ACS Nano 2024, 18, 11025−11041

Other approaches have aimed to eliminate myeloid cells in the TME (i.e., liposomal chlodronate),[61] or abrogate the immunosuppressive actions of myeloid cells on lymphocytes (i.e., checkpoint inhibitors; durvalumab).[62] Yet single-solution target-based therapies still face many challenges.[63,64] In addition, targeting single cell types can be inefficient, as the TME is hallmarked by complex and plastic interactions of numerous malleable immune cell types that may compensate for each other.[65] Pulmonary SPION-CCPM instillation targets ∼70% of the $CD45^+$ immune compartment in lung tumor-bearing mice, including monocytes, macrophages, granulocytes, and dendritic cells, and induces multifaceted alterations of the myeloid and lymphoid immune cell architecture. Macrophages were reduced in SPION-CCPM-instilled mice compared to control mice and were shown to have a pro-inflammatory state hallmarked by increased MHC II and CD86 levels. Interestingly, reprogramming of the TME by SPION-CCPMs significantly increased the frequency of T cells ($CD8^+$) by approximately 2-fold, providing an additional mechanism for reducing tumor growth. Similar effects have been observed by other therapies, such as the monoclonal antibody emactuzumab, which blocks colony-stimulating factor 1 (CSF1), and was shown to reduce the frequency of TAMs, polarize the remaining TAM populations and increase the ratio of $CD8^+/CD4^+$ T cells in the TME, thus enhancing therapy responses.[66]

Altogether, we show that SPION-CCPMs therapy alters the TME in an *Eml4-Alk* lung cancer model either directly by rewiring the phenotypes of iron-containing cells or indirectly by affecting their communication with other immune cell types and reducing cancer cell proliferation as a result. This clinically relevant work provides therapeutic opportunities based on nanoparticles. The ability of SPION-CCPMs to target and polarize many different cell types makes SPION-CCPM therapy an attractive option for previously unresponsive lung tumors.

CONCLUSIONS

We show that application of SPION-CCPMs in an *Eml4-Alk* lung cancer mouse model induces phenotypic alterations in those cells that accumulate iron and rewires the communication of immune cells in the TME such that cancer cell proliferation is reduced. This clinically relevant work provides therapeutic opportunities based on nanoparticles for previously unresponsive lung tumors.

Study Strengths. SPION-CCPMs are synthesized to contain disulfide bonds that can be rapidly cleaved inside phago- and pinocytic compartments of macrophages, allowing for rapid particle disintegration and the release of the SPIONs. Compared to the application of SPIONs or feraheme, SPION-CCPMs exert a much stronger pro-inflammatory response in macrophages.[29] SPION-CCPMs applied as an adjuvant iron-based therapy reshape the immunosuppressive environment exerted by *Eml4-Alk* lung cancer cells and significantly delay tumor growth, after first line therapy with a TKI. This study presents a therapeutic strategy combining TKIs and SPION-CCPMs and is expected to fuel a wave of therapies that combine iron oxide nanoparticles with other conventional cancer therapies.

Study Limitations. Despite the highly valuable insights gained, this study shows some potential limitations. First, the sample sizes of mice were constrained by ethical considerations in Germany. In one case, the restricted sample size was insufficient to yield statistically significant results. Second, this study analyzed an *Eml4-Alk* lung cancer mouse model and one TKI treatment. Thus, it remains unknown whether SPION treatment is equally efficient in other lung cancer types or when combined with different drugs, such as conventional chemotherapies or checkpoint inhibitors. Third, SPION administration in mice was confined to intratracheal instillation. Intravenous injection proved unsuitable due to SPION accumulation in the spleen and liver, with only limited lung impact. Intratracheal instillation offered a more targeted approach with minimal side effects, offering potential for future developments such as nebulization or inhaler methods.

METHODS/EXPERIMENTAL

Unless stated otherwise, solvents were purchased from Sigma-Aldrich. THF and *n*-hexane were dried over Na and freshly distilled prior to use. DMF was bought from Acros (99.8%, extra dry over a Molecular Sieve), freshly freeze-pumped prior to use to remove residual dimethyl amine, and handled in the absence of light. HFIP was purchased from Fluorochem, and deuterated solvents were used as received. Milli-Q water was prepared using a Milli-Q Reference A+ System. Water was used at a resistivity of 18.2 $M\Omega\cdot cm^{-1}$ and total organic carbon of <5 ppm. Diphosgene was purchased from Alfa Aesar. Sarcosine was bought from Sigma-Aldrich and dried in vacuum before NCA synthesis. *N-tert*-butoxycarbonyl (Boc)-1,2-diaminoethane and *N,N*-diisopropyl ethylamine (DIPEA) were purchased from Sigma-Aldrich, fractionally distilled, and stored at −78 and −20 °C, respectively. Oleic acid coated iron oxide nanoparticles were obtained from Sanofi-Aventis Deutschland GmbH, as well as obtained from Ocean Nanotech. D,L-Lipoic and was bought from TCI Europe. Pentafluorophenyl trifluoroacetate, tris(2-carboxyethyl)phosphine (TCEP·HCl) and acetic acid anhydride were obtained from Sigma-Aldrich and used without further purification. Cyanine 5 NHS Ester was obtained from Lumiprobe GmbH.

SPION CCPM Synthesis. The synthesis of block copolymers and CCPMs was performed as previously published.[31] The synthesis of SPION CCPMs was performed according to Bauer et al.[29] At first, oleic acid-coated SPIONs (β = 5.8 g L^{-1}, 9.0 mL) dispersed in hexanes were precipitated into 40 mL of ethanol, sonicated for 15 min, and sedimented (4500 rpm, 15 min, 20 °C). The pellet was resuspended in 5.0 mL of chloroform, sonicated for 30 min, precipitated in 45 mL of ethanol, and sedimented (4500 rpm, 15 min, 20 °C) to remove excess oleic acid. SPIONs were resuspended in 20 mL of chloroform, and a polymer solution in DMSO/$CHCl_3$ (1:2; β = 5.0 g L^{-1}, 10 mL) was added dropwise. The resulting clear brown solution was placed in a dialysis bag (MWCO 3.5 kDa) and dialyzed against $CHCl_3$, followed by dialysis against DMSO. The solution was diluted with DMSO by a factor of 2 and dialyzed against Milli-Q water to obtain SPION-loaded polymeric micelles. The obtained micelles were filtered through a PVDF 0.45 μm filter and concentrated to a total volume of 8.0 mL by spin filtration (Amicon Ultra-15, MWCO 3.0 kDa, 4500 rpm, 20 °C). For core cross-linking, D,L-lipoic acid (8.0 mg, 39.1 mmol, 0.5 equiv per pCys(SO_2Et) repeating unit) was dissolved in ethanol (5.0 g L^{-1}) and treated with tris(2-carboxyethyl)phosphine hydrochloride (11.2 mg, 39.1 mmol, 50 g L^{-1} in Milli-Q water) for 18 h, yielding dihydro lipoic acid. The cross-linker solution was added to the micelle solution, and the reaction mixture was placed on a benchtop shaker for 24 h. Subsequently, excess cross-linker and residual oleic acid were removed by dialysis (MWCO 3.5 kDa) against DMSO/Milli-Q water mixtures (1:1) followed by dialysis against Milli-Q water yielding a clear light brown solution. For dye conjugation, the SPION-CCPM solution was adjusted to pH 7.4 using 1 m sodium hydrogen carbonate solution, Cy5-NHS ester (540 μg, 0.3 equiv per polymer, 25 g L^{-1} in DMSO) was added, and the solution was stirred at room temperature for 72 h. Upon addition of the blue dye solution, the particle solution turned dark green immediately. The excess dye was removed by repetitive extraction with dichloromethane, followed by dialysis against ethanol/Milli-Q water mixtures (1:1) and Milli-Q water (MWCO 6−8 kDa). To remove the free polymer, Cy5-labeled SPION-CCPMs (SPION-$CCPM^{Cy5}$) were purified by repetitive spin filtration (Amicon Ultra-15, MWCO 100

https://doi.org/10.1021/acsnano.3c08335
ACS Nano 2024, 18, 11025−11041

kDa, 3000 rpm, 20 °C), and finally concentrated to a total volume of 8.5 mL, yielding 23 mg of SPION-CCPM^{Cy5} (overall yield 23%).

Dynamic Light Scattering. Single-angle DLS measurements were performed with a ZetaSizer Nano ZS instrument (Malvern Instruments Ltd., Worcestershire, U.K.) equipped with a He−Ne laser (λ = 632.8 nm) as the incident beam. All measurements were performed at 25 °C and a detection angle of 173°, unless stated otherwise. Disposable polystyrene cuvettes (VWR, Darmstadt, Germany) were used for single-angle DLS measurements. Disposable folded capillary cells (Malvern Instruments Ltd., Worcestershire, U.K.) were employed for zeta potential measurements. Zeta potential measurements were conducted in solutions containing 3 mm of sodium chloride. Cumulant size, polydispersity index (PDI), and size distribution (intensity weighted) histograms were calculated based on the autocorrelation function of the samples, with automated position and attenuator adjustment at multiple scans. The derived count rate was used for the aggregation and dissociation experiments.

Transmission Electron Microscopy. TEM was performed on a FEI Tecnai G2 Spirit microscope equipped with a Gatan US1000 2k × 2k CCD camera and LaB_6 cathode operated at 120 kV. Images were recorded using freshly glow discharged carbon coated copper grids (CF300-Cu, 300 mesh). For nonstained samples, 5 μL of nanoparticle solution (β = 50 mg·L^{-1} in Milli-Q water) was drop-coated on the TEM grid surface and removed with a filter paper after 1 min. For negatively stained samples, 5 μL of nanoparticle solution (β = 50 mg·L^{-1} in Milli-Q water) was drop-coated on the TEM grid and removed with a filter paper after 1 min. Next, 5 μL of uranyl acetate solution (2 wt % in ethanol) was added and removed after 15 s incubation time. All sample-deposited grids were air-dried overnight before measurement. Software ImageJ 1.52h (National Institutes of Health, U.S.A.) was used for image evaluation.

For cryogenic TEM (cryo-EM) sample preparation, 3 μL of the nanoparticle solution (5 mg/mL, in Milli-Q water) were applied to freshly glow-discharged carbon grids with a copper 200 mesh (Quantifoil Micro Tools GmbH). Grids were plunge-frozen in liquid ethane using a Vitrobot Mark IV (Thermo Fisher Scientific) set at 22 °C, 100% humidity, and 2.5 s blotting time. Samples were imaged in a Talos L120C transmission electron microscope equipped with a LaB6 filament operating at a 120 kV accelerating voltage. Images were recorded using a Ceta camera.

Cell Lines. Lewis lung carcinoma cells (LLC) were cultured in Roswell Park Memorial Institute Medium (RPMI; 21875091, Life-Technologies) containing 10% fetal bovine serum (FBS; 10500064, LifeTechnologies), 1% penicillin/streptomycin, and supplemented with 10 ng mL^{-1} M-CSF (M9170, Sigma-Aldrich).

Eml4-Alk tumor cells were derived from mTmG,[67] CCSP-Cre[68] mice maintained on an FVB background, and which had been previously instilled with an *Eml4-Alk* adenovirus generated by Maddalo et al.[44] In these mice, the Cre expression in CCSP expressing cells represses the expression of membranous tdTomato (mT) and induces the expression of membranous GFP (mG), labeling the cells in green. For the establishment of the cell line, a single nodule was isolated from the lung of a tumor-bearing mouse, digested with 50 U/mL Dispase, and cultured in DMEM with 10% FBS. Cells were then maintained in RPMI (21875091, LifeTechnologies) with 10% FBS, 1% penicillin/streptomycin, and 10 ng/mL m-CSF (M9170, Sigma-Aldrich).

Bone Marrow-Derived Macrophage Isolation, Differentiation, and Coculture. Bone marrow-derived macrophages (BMDMs) were isolated as previously described.[69] Briefly, bone marrow cells were flushed from the tibia and femurs of C57BL/6N or FVB wild-type adult mice with ice cold Hanks' Balanced Salt Solution (HBSS) and filtered through a 70 μm cell strainer. BMDMs were then plated at a density of 3.5×10^5 cells/mL and differentiated using RPMI supplemented with 10 ng mL^{-1} M-CSF (M9170, Sigma-Aldrich), 10% FBS, and 1% penicillin/streptomycin (Gibco) for 1 week. For each experiment, BMDMs were prepared from 3 or 4 independent mice. Then, cancer cells were plated with BMDMs at a 2:1 ratio, and cultures were left untreated or treated with SPION-CCPMs in a concentration that corresponds to 100 μM iron, with CCPMs at a concentration that matched the shell mass of the SPION-CCPMs. For transwell culturing, cancer cells were plated into 3 μm transwell inserts which were then placed into 6-well culturing plates containing BMDMs. For proliferation assays, cancer cells were stained with 5 μM carboxyfluorescein succinimidyl ester (CFSE)[70] using the CellTrace Yellow Cell Proliferation Kit (C34573, Life Technologies) prior to coculturing. The proliferation index was calculated from proliferation analysis using FlowJo Software and represented as fold change versus NT condition. For antibody neutralization, an anti-TNFα monoclonal antibody at 100 ng/mL (MP6-XT22, eBioscience) and an IL-1β monoclonal antibody at 2 μg/mL (MP5−20F3, eBioscience) were used. For iNOS inhibition, 100 μM 1400W dihydrochloride (1415/10, Biotechne) was used. For other assays, 5 nM erastin (329600-5MG, Sigma-Aldrich), 10 nM liproxstatin (HY-12726-5 mg, Hoelzel Diagnostika), 10 μM Q-VD-OPh (HY-12305-5 mg, Hoelzel Diagnostika), 0.25 mM 3-methyladenine (HY-19312-100 mg, Hoelzel Diagnostika), and 0.2 μM necrostatin-1 (sc-200142, Santa Cruz Biotechnology) were used on cocultures of BMDMs and cancer cells for the indicated times.

Flow Cytometry. BMDMs and cocultured cancer cells were incubated with Fc-γ receptor blocking solution (mouse, 130−092−575, Miltenyi Biotec) prior to staining with probes, antibodies, or viability dyes. For probe staining, samples were incubated in the dark for 10 min at 4 °C with H2DCFDA (D-399, Life Technologies) or BODIPY 581/591 (D3861, Life Technologies) probes. Subsequently, antibodies for macrophage cell surface markers were added for 30 min at 4 °C (see Table S1 for Supporting Information). Samples were stained for viability using LIVE/DEAD Fixable near-IR dead cell stain kit (L34975, Life Technologies) before fixation (10 min at RT in 4% paraformaldehyde), subsequent washing with PBS and analysis on a flow cytometer (Cytotek Aurora) and the proportion of live versus dead was used to calculate viability overtime. Live samples were stained for viability with 0.1 μg/mL DAPI (SBA-0100−20, Biozol) prior to analysis. For propidium iodide staining, samples were fixed for 30 min at 4 °C in ice cold 70% ethanol, washed with PBS and resuspended in a solution of 10 μg/mL propidium iodide (ab14083, Abcam) and 5 μg ribonuclease (12091021, Life Technologies).

Mouse lungs were resected and washed in PBS. Samples were dissociated into single cells using a mouse lung dissociation kit (Miltenyi Biotech, 130−095−927) in a gentleMACS Octo Dissociator (Miltenyi Biotech, 130−095−937). Cells were stained with antibodies; see Table S1, Supporting Information. For cell cycle analysis, lung single cells were incubated with CD45 microbeads (Miltenyi Biotec, 130−110−618) following the manufacturer's instructions and passed through the LS columns (Miltenyi Biotec, 130−042−401). The magnetically labeled immune cells were flushed out of the columns and processed for mRNA quantitative analysis. The flow-through was incubated with CD31 microbeads (Miltenyi Biotec, 130−097−418) following the manufacturer's instructions to remove endothelial cells and passed through LS columns. The flow-through was then stained with propidium iodide following the above-described methods.

Data were acquired using the Cytotek Aurora flow cytometer at the EMBL Flow Cytometry Core Facility and analysis was performed using the FlowJo Software (Tree Star Inc.). The expression of surface markers in mouse lung cells and BMDMs was calculated by subtracting the geometric median fluorescence intensity (MFI) of cells stained with the isotype-matched antibody from the MFI of those stained with the specific antibody and was shown as fold-change compared to the nontreated (NT) or PBS control. Unsupervised clustering analysis was done by concatenating biological replicates and using FlowJo plugin FlowSOM or Phenograph.

Protein Extraction and Western Blotting. Protein lysates were obtained by homogenizing cells in a RIPA buffer supplemented with protease inhibitors (Roche Diagnostics). Protein concentration was measured by using the DC Protein Assay Kit II system (5000112, Bio-Rad). 50 μg of total protein extracts were separated by 12% SDS-PAGE and analyzed by Western blotting using antibodies against anti-Ferritin Heavy Chain 1 (FtH1; ab183781, Abcam) or Ferritin-L Antibody (FtL; ab69090, Abcam). β-Actin (A1978-200UL, Sigma-Aldrich) was used as a loading control. Western blot images were quantitatively acquired with the Vilber Lourmat Fusion-FX Chemiluminescence system (Eberhardzell) and analyzed by using Fiji. Densitometric analysis was

https://doi.org/10.1021/acsnano.3c08335
ACS Nano 2024, 18, 11025−11041

done by calculating the ratio of FtL or FtH1 levels to actin levels and then represented as fold change vs the nontreated (NT) sample.

RNA Extraction, Reverse Transcription, and Quantitative Real-Time PCR Analysis. RNA was extracted from lung tissue using Trizol (Life Technologies) or from cultured cells using the RNeasy Mini Kit (74134, Qiagen). A total of 0.5 to 1 μg of total RNA was reverse transcribed by using RevertAid H Minus Reverse Transcriptase (FERMEP0452, Thermo Scientific), random primers (48190-011, Invitrogen), and dNTPs (R0193, ThermoScientific). SYBR green qRT-PCR was performed on a Step One Plus Real-Time PCR System (Applied Biosystems, California, U.S.A.). Primers and probes were designed using the ProbeFinder software (www.roche-applied-science.com; see Table S2, Supporting Information). Differences in relative quantity were shown as fold changes compared to the control condition (untreated cells, NT).

Sample Preparation and Protein Digestion. For proteomic analysis of cocultured cells, cells were incubated with F4/80 microbeads (Miltenyi Biotec, 130−110−443) following the manufacturer's instructions and passed through the MS columns (Miltenyi Biotec, 130−042−201) to separate macrophages from cancer cells. Both cancer cells and BMDMs were lysed in lysis buffer 1, containing 50 mM Tris pH 7.4, 150 mM NaCl, 1 mM EDTA pH 8.8, 0.1% deoxycholic acid NA-salt, 0.5 mM Na_3VO_4, 2.5 mM NaF, 4% SDS, 1 μg/mL aprotinin, and 0.1 mg/mL 4-(2-aminoethyl)-benzenesulfonyl fluoride hydrochloride. Total cell lysates were then sonicated on ice using a sonication probe (30 s; 75% amplitude; 0.1-on 0.5-off cycles). Samples were centrifuged for 10 min at 14000 rpm and 20 °C, and the supernatant was transferred to a new vial. The remaining pellet was suspended in lysis buffer 2 containing 100 mm triethylammonium bicarbonate (TEAB), 8 M urea, 2% SDS, 1 μg/mL AP, 0.1 mg/mL AEBSF, incubated for 20 min at 37 °C, and sonicated using a sonication probe (30 s; 75% amplitude; 0.1-on 0.5-off cycles) on ice. For each sample, supernatant and pellets were combined, and total protein concentration was assessed by the BCA Assay (Pierce), performed according to the manufacturer. In total, 5 μg of protein per sample was used for further processing. Samples presenting low protein concentration (<0.2 μg/μL) were dried by vacuum centrifugation, suspended in 20 μL of 100 mM TEAB, and used for further processing. All sample volumes were corrected with 100 mM TEAB. The disulfide bonds of proteins were reduced with 40 mM Tris(2-carboxyethyl) phosphine (TCEP) and then alkylated with 10 mM chloroacetamide (CAA) for 60 min at 37 °C. Protein digestion and cleanup were performed using an adapted version of the automated paramagnetic bead-based single-pot, solid-phase-enhanced sample-preparation (Auto-SP3) protocol[71] on the Bravo liquid handling platform (Agilent). Briefly, for bead preparation, Sera-Mag Speed Beads A and B (Ge Healthcare) were vortexed until the pellet was dissolved. The suspension was placed on a magnetic rack, and after one min, the supernatant was removed. The beads were taken off the magnetic rack and suspended in water. This procedure was repeated three times. A total of 10 μL of bead A was combined with 10 μL of bead B, and the final volume was corrected to 100 μL with H_2O. To each sample, a total of 5 μL of A+B beads were added. To induce the binding of the proteins to the beads, ethanol was added to each sample to a final 50% concentration (v/v). Samples were then incubated for 15 min at room temperature and 800 rpm. After the incubation step, samples were placed again on a magnetic rack, and after one min, the supernatant was removed. Samples were taken off the magnetic rack and suspended in 80% ethanol. This procedure was repeated three times. Finally, samples were reconstituted in 100 mM TEAB buffer containing trypsin (enzyme/protein ratio of 1:25) and digested overnight on a shaker at 37 °C and 1000 rpm. After digestion, the recovered peptides were dried by vacuum centrifugation and stored at −80 °C until use.

LC-MS/MS Analysis. Nanoflow LC-MS/MS was performed by coupling an EASY-nLC 1200 to an Orbitrap Exploris 480 mass spectrometer (Thermo Scientific). Peptide samples were dissolved in 15 μL of loading buffer (0.1% formic acid (FA), 2% ACN in MS-compatible H_2O), and 2 μL were injected for each analysis. Peptides were delivered to an analytical column (75 μm × 30 cm, packed in-house with Reprosil-Pur 120 C18-AQ, 1.9 μm resin, Dr. Maisch) at a flow rate of 3 μL/min in 98% buffer A (0.1% FA in MS-compatible H_2O). After loading, peptides were separated using a 120 min gradient from 2% to 38% of buffer B (0.1% FA, 80% ACN in MS-compatible H_2O) at a 350 nL/min flow rate. The Orbitrap Exploris 480 mass spectrometer was operated in data-dependent mode (DDA), automatically switching between full scan MS and MS2. Full scan MS spectra were acquired in the Orbitrap at 60 000 (m/z 200) resolution after accumulation to the set target value of 300% (100% = $1e^6$). Tandem mass spectra were generated for up to 20 peptide precursors in the orbitrap (isolation window of 1.0 m/z) for fragmentation using higher energy collisional dissociation (HCD) at normalized collision energy (N)CE of 30%. MS2 spectra were acquired in the Orbitrap at a resolution of 15000 with a target value of 100% ($1e^5$) charges after accumulation for a maximum of 22 ms.

Database Search and Proteomic Data Analysis. Raw MS spectra were processed by MaxQuant (version 2.0.1.0) for peak detection and quantification. MS/MS spectra were searched against the Uniprot *Mus musculus* reference proteome database (downloaded on June 26th, 2019) by the Andromeda search engine enabling contaminant detection and the detection of reversed versions of all sequences with the following search parameters: Carbamidomethylation of cysteine residues as fixed modification and acetyl (Protein N-term), oxidation (M) as variable modifications. Trypsin/P was specified as the proteolytic enzyme with up to three missed cleavages allowed. Matching between runs was allowed to align replicates belonging to the same group. The time-dependent recalibration algorithm of MaxQuant determined the mass accuracy of the precursor ions. The maximum false discovery rate (FDR) for proteins and peptides was 0.01, and a minimum peptide length of eight amino acids was required; all other parameters were the default settings. The MaxQuant output was further processed with the MSPypeline[72] to generated a Quality Control report and descriptive plots. Additionally, the LFQ intensities were used for differential expression analysis. Statistical significance was assessed using the limma package.[73]

Pathway enrichment analysis was performed through Metascape[74] (Web server: https://metascape.org) using default settings.

GSH Assay. BMDMs, cancer cells, or BMDMs and cancer cells were plated at a 2:1 ratio in 96-well plates and incubated for 48 h following the addition of treatments. After the removal of supernatants, cells were lysed and total GSH levels were evaluated using a GSH colorimetric assay (EIAGSHC, LifeTechnologies) following the manufacturer's protocol.

Mice and Adenoviral Infection. FVB wild-type mice were purchased from Janvier Laboratories. All animal experiments were performed at the DKFZ animal facilities, following the guidelines of EU animal laws and with ethical approval from Baden-Wurttemberg Animal Welfare and ethical review bodies under protocol number G214/19.

To induce *Eml4-Alk* tumors in the lung, mice older than 6 weeks were anesthetized by intraperitoneal injection of 100 μg/g ketamine and 14 μg/g xylazine and intratracheally instilled with *Eml4-Alk* adenovirus purchased from Viraquest. After 6 weeks of quarantine to allow for viral clearance, nanoparticle or PBS treatments were carried out in the following manner: mice were anesthetized by intraperitoneal injection of 100 μg/g ketamine and 14 μg/g xylazine and intratracheally instilled with SPION-CCPM (10 mg/kg of iron to body weight) or PBS in a final volume of 30 μL. The treatment was administered up to a maximum of 4 times every 4 days. Mice were monitored for signs of stress or suffering, while tumor growth was monitored by μCT. Mice were sacrificed by intraperitoneal injection of xylazine 42 mg/kg and ketamine 300 mg/kg.

Crizotinib treatment (100 mg/kg) consisted of daily administrations by oral gavage for 5 days with a two-day break until tumors completely regressed or mice became noncompliant. Treatment began when the tumor burden reached 30 mm.[3] SPION-CCPM (10 mg/kg of iron to body weight) or PBS treatment occurred in a final volume of 30 μL. Treatments were performed as outlined for the individual experiments, e.g., 2 times with a 6-day difference. Tumor growth was monitored by μCT 2 weeks later.

https://doi.org/10.1021/acsnano.3c08335
ACS Nano 2024, 18, 11025−11041

Tissue Non-Heme Iron Measurement. Mouse tissues were measured for nonheme iron content using the bathophenantroline method and calculated against dry weight of tissue.[75]

Serum Iron Measurement. For the analyses of serum parameters, blood was collected in tubes with a gel clot activator for serum separation. After 30 min of RT incubation, samples were centrifuged for 10 min at 10000 rcf. Serum iron concentration was determined using the SFBC and UIBC kit (Biolabo 97408, 80008) following manufacturer's instructions.

Immunostainings. For immunostainings, cells were plated on 13 mm glass coverslips (Life Technologies #A1048301), treated for the indicated times, fixed with 4% paraformaldehyde, and permeabilized using 0.1% Triton-100X PBS Tween 0.01%. Samples were then blocked with 5% milk in PBS-T and stained with the primary antibody Ki67 (Medac, 275R-18) or γ-H2AX 1:200 (Santa Cruz, sc-517348) overnight at 4 °C. After washing, samples were incubated with the secondary antibody donkey anti-Rabit IgG (H+L) Alexa Fluor 568 (Abcam, ab175470) and mounted using ProLong Diamond Antifade Mountant with DAPI (Life Technologies, P36966). Pictures were acquired in a Zeiss Cell Observer system and analyzed using the Cellprofiler software[76] (Broad Institute) to quantify nanoparticle ($Cy5^+$) fluorescence, cancer cell (GFP^+) fluorescence, $Ki67^+$, or γ-$H2AX^+$ nuclear fluorescence signals.

Tissues were incubated with 10% formalin (Sigma, HT501128) on a tube rocker for 24 h before further processing in a tissue processor (Leica ASP300S). Tissues were then embedded in paraffin blocks and sectioned at a 3 μm thickness. For immunohistochemical staining, ABC kits (Vector Laboratories, PK-6101, PK-6104) and the Mouse on Mouse (M.O.M.) Basic Kit (Vector Laboratories, BMK-2202), together with Diaminobenzidine (DAB) peroxidase substrate kit (Vector Laboratories, SK-4100) were used according to the manufacturer's instructions. Primary antibodies used were: Ki67 (Medac, 275R-18), p21 1:50 (Santa Cruz, SC-6246), and γ-H2AX 1:200 (Santa Cruz, sc-517348), CD4 1:500 (Abcam, ab183685), CD8 1:100 (Thermo Scientific, 14−0808−80). Images were taken in a TissueGnostic TissueFAX system and analyzed by using the StrataQuest software (TissueGnostic).

Perls' Prussian Blue Staining and DAB-enhanced Perls' staining. Formalin-fixed paraffin-embedded tissues were stained with Accustain Iron Stain (HT20-1KT, Sigma-Aldrich) following manufacturer's instructions, developed using a DAB peroxidase substrate kit (Vector Laboratories, SK-4100) and counterstained with Fast Red (Sigma-Aldrich, N8002-5G). Samples were mounted using DPX Mountant (06522, Sigma). Images were taken in a Tissuegnostic TissueFAX system.

μCT Imaging. μCT imaging was performed using the Inveon multimodality μPET/SPECT/CT system (Siemens Medical Solutions, Knoxville, U.S.A.). Acquisitions covering the thorax and lungs were performed by using a tube voltage of 80 kV and a tube current of 500 μA. A total of 360 projections were acquired over 360°, with an integration time of 200 ms each. The detector was operated using a 4 × 4 binning mode, resulting in a resolution of approximately 100 μm in the center of rotation. Image reconstruction with isotropic resolution was performed using the Feldkamp algorithm with a Shepp-Logan kernel onto a 512 × 512 × 928 grid with appropriately sized voxels. Image analysis was done using ImageJ. Tumor volume was calculated using the following formula: $V = 4/3\pi r^3$, where r = tumor radius, determined by measuring the diameter of each tumor.

Data Availability. The mass spectrometric raw data files, along with the MaxQuant result files, are available on the proteomeXchange platform,[77] http://www.proteomexchange.org, under the accession number PXD040145.

Statistics and Reproducibility. Data are shown as mean ± SEM. Statistical analyses were performed using Prism v9 (GraphPad Software, La Jolla, CA). The statistical information for experiments is detailed in the text, figure legends, and figures. Mice were randomized to different groups without selection. The investigators were not blinded to allocation during the experiments and outcome assessment. The sample size for animal experimentation was predetermined using published data[27] and the Power and Sample Size software and are indicated in the figure legends.

ASSOCIATED CONTENT

Supporting Information

The Supporting Information is available free of charge at https://pubs.acs.org/doi/10.1021/acsnano.3c08335.

Figure S1, SPION-CCPM uptake in cocultures, EML4-Alk proteomics, gene analysis, γ-H2AX microscopy, Nqo1/Gclc RT-PCR, and GSH assays; Figure S2, cell viability, lipid peroxidation, Gpx4 RT-PCR, LDH, drug assays, antibody neutralization assay, and coculture proteomics; Figure S3, SPION-CCPM intratracheal instillation data in mice; Figure S4, supplementary results for Figures 4 and 5; Table ST1, RT-PCR primer pairs; Table ST2, flow cytometry antibodies (PDF)

AUTHOR INFORMATION

Corresponding Authors

Matthias W. Hentze − *Molecular Medicine Partnership Unit (MMPU), Otto-Meyerhof-Zentrum, 69120 Heidelberg, Germany; European Molecular Biology Laboratory (EMBL), 69117 Heidelberg, Germany*; Email: hentze@embl.org

Rocío Sotillo − *Division of Molecular Thoracic Oncology, German Cancer Research Center (DKFZ), 69120 Heidelberg, Germany; German Center for Lung Research (DZL) and Translational Lung Research Center Heidelberg (TRLC), 69120 Heidelberg, Germany; German Consortium for Translational Cancer Research (DKTK), 69120 Heidelberg, Germany*; Email: r.sotillo@dkfz-heidelberg.de

Martina U. Muckenthaler − *Department of Pediatric Hematology, Oncology, Immunology and Pulmonology, Heidelberg University Hospital, 69120 Heidelberg, Germany; Molecular Medicine Partnership Unit (MMPU), Otto-Meyerhof-Zentrum, 69120 Heidelberg, Germany; German Center for Lung Research (DZL) and Translational Lung Research Center Heidelberg (TRLC), 69120 Heidelberg, Germany; German Centre for Cardiovascular Research (DZHK), 69120 Heidelberg/Mannheim, Germany*; orcid.org/0000-0002-3778-510X; Email: martina.muckenthaler@med.uni-heidelberg.de

Authors

Natalie K. Horvat − *Department of Pediatric Hematology, Oncology, Immunology and Pulmonology, Heidelberg University Hospital, 69120 Heidelberg, Germany; Molecular Medicine Partnership Unit (MMPU), Otto-Meyerhof-Zentrum, 69120 Heidelberg, Germany; Ruprecht Karl University of Heidelberg, 69120 Heidelberg, Germany*

Sara Chocarro − *Division of Molecular Thoracic Oncology, German Cancer Research Center (DKFZ), 69120 Heidelberg, Germany; Ruprecht Karl University of Heidelberg, 69120 Heidelberg, Germany*

Oriana Marques − *Department of Pediatric Hematology, Oncology, Immunology and Pulmonology, Heidelberg University Hospital, 69120 Heidelberg, Germany; Molecular Medicine Partnership Unit (MMPU), Otto-Meyerhof-Zentrum, 69120 Heidelberg, Germany*

Tobias A. Bauer − *Leiden Academic Centre for Drug Research (LACDR), Leiden University, 2333CC Leiden, The Netherlands*

Ruiyue Qiu − *Department of Pediatric Hematology, Oncology, Immunology and Pulmonology, Heidelberg University Hospital, 69120 Heidelberg, Germany*
Alberto Diaz-Jimenez − *Division of Molecular Thoracic Oncology, German Cancer Research Center (DKFZ), 69120 Heidelberg, Germany; Ruprecht Karl University of Heidelberg, 69120 Heidelberg, Germany*
Barbara Helm − *Division of Systems Biology of Signal Transduction, German Cancer Research Center (DKFZ), 69120 Heidelberg, Germany; German Center for Lung Research (DZL) and Translational Lung Research Center Heidelberg (TRLC), 69120 Heidelberg, Germany*
Yuanyuan Chen − *Division of Molecular Thoracic Oncology, German Cancer Research Center (DKFZ), 69120 Heidelberg, Germany*
Stefan Sawall − *X-ray Imaging and CT, German Cancer Research Center (DKFZ), 69120 Heidelberg, Germany*
Richard Sparla − *Department of Pediatric Hematology, Oncology, Immunology and Pulmonology, Heidelberg University Hospital, 69120 Heidelberg, Germany*
Lu Su − *Leiden Academic Centre for Drug Research (LACDR), Leiden University, 2333CC Leiden, The Netherlands;* orcid.org/0000-0001-8207-756X
Ursula Klingmüller − *Division of Systems Biology of Signal Transduction, German Cancer Research Center (DKFZ), 69120 Heidelberg, Germany; German Center for Lung Research (DZL) and Translational Lung Research Center Heidelberg (TRLC), 69120 Heidelberg, Germany; German Consortium for Translational Cancer Research (DKTK), 69120 Heidelberg, Germany*
Matthias Barz − *Leiden Academic Centre for Drug Research (LACDR), Leiden University, 2333CC Leiden, The Netherlands; Department of Dermatology, University Medical Center of the Johannes Gutenberg University Mainz, 55131 Mainz, Germany;* orcid.org/0000-0002-1749-9034

Complete contact information is available at: https://pubs.acs.org/10.1021/acsnano.3c08335

Author Contributions

⬢These authors contributed equally to this work (N.K.H. and S.C.).

Author Contributions

N.K.H.: Project conceptualization; N.K.H. and S.C.: Contributed equally to project design and investigation, data curation, formal analysis, and writing: original draft, review, and editing; O.M.: Project conceptualization, investigation, formal analysis, and writing: review and editing; R.Q.: Project investigation; T.A.B., L.S., and M.B.: Nanoparticle reagent construction and characterization; A.D.: Cell line generation; B.H. and U.K.: Proteomic data analysis; Y.C.: Data analysis; S.S.: Method development of mouse lung tumor detection by μCT; M.W.H and M.U.M.: Contributed equally to project conceptualization; M.W.H., M.U.M., and R.S.: Contributed equally to project design, supervision, and writing: review and editing.

Funding

This work was partially supported by the Deutsches Zentrum für Lungenforschung (DZL, German Center for Lung Research # 82DZL004B4) to M.U.M., R.S., and U.K. O.M. received support from the European Hematology Association (RG66) and by an Olympia Morata-Programm Fellowship given by the Medical Faculty of the University of Heidelberg. M.U.M. and M.B. acknowledge support from the Deutsche Forschungsgemeinschaft (FerrOs-FOR5146; GRK2727; SPP2306; SFB1066-3).

Notes

The authors declare the following competing financial interest(s): N.K.H., T.A.B., M.U.M., M.W.H., and M.B. submitted a patent application related to the data presented in this manuscript.

ACKNOWLEDGMENTS

We would like to thank the DKFZ Core Facilities of Light Microscopy and the Small Animal Imaging Center for the technical assistance and the Central Animal Laboratory for animal care and husbandry. Authors would also like to acknowledge the EMBL Flow Cytometry Core Facility, especially Dr. Malte Paulsen and Dr. Diana Ordonez, for training, discussions, and technical assistance. We thank Dr. Sandro Altamura, Dr. Silvia Colucci, and Dr. Francesca Vinchi for insightful discussions, inspiration, and support spanning the course of this study. Authors would like to thank Dr. Jessica Konen for scientific consulting and Prof. Annette Kopp-Schneider for help with statistical analyses. Schemes were generated using BioRender.com.

REFERENCES

(1) Sung, H.; Ferlay, J.; Siegel, R. L.; Laversanne, M.; Soerjomataram, I.; Jemal, A.; Bray, F. Global Cancer Statistics 2020: GLOBOCAN Estimates of Incidence and Mortality Worldwide for 36 Cancers in 185 Countries. *Ca Cancer J. Clin* **2021**, *71* (3), 209−249.
(2) Sica, A.; Mantovani, A. Macrophage Plasticity and Polarization: In Vivo Veritas. *J. Clin Invest* **2012**, *122* (3), 787−795.
(3) Franklin, R. A.; Li, M. O. Ontogeny of Tumor-Associated Macrophages and Its Implication in Cancer Regulation. *Trends Cancer* **2016**, *2* (1), 20−34.
(4) Sedighzadeh, S. S.; Khoshbin, A. P.; Razi, S.; Keshavarz-Fathi, M.; Rezaei, N. A Narrative Review of Tumor-Associated Macrophages in Lung Cancer: Regulation of Macrophage Polarization and Therapeutic Implications. *Transl Lung Cancer Res.* **2021**, *10* (4), 1889−1916.
(5) Condeelis, J.; Pollard, J. W. Macrophages: Obligate Partners for Tumor Cell Migration, Invasion, and Metastasis. *Cell* **2006**, *124* (2), 263−266.
(6) Shi, L.; Wang, L.; Hou, J.; Zhu, B.; Min, Z.; Zhang, M.; Song, D.; Cheng, Y.; Wang, X. Targeting Roles of Inflammatory Microenvironment in Lung Cancer and Metastasis. *Cancer Metast Rev.* **2015**, *34* (2), 319−331.
(7) Calles, A.; Riess, J. W.; Brahmer, J. R. Checkpoint Blockade in Lung Cancer With Driver Mutation: Choose the Road Wisely. *Am. Soc. Clin Oncol Educ Book* **2020**, *40* (40), 372−384.
(8) Cooper, A. J.; Sequist, L. V.; Lin, J. J. Third-Generation EGFR and ALK Inhibitors: Mechanisms of Resistance and Management. *Nat. Rev. Clin Oncol* **2022**, *19* (8), 499−514.
(9) Schenk, E. L. Narrative Review: Immunotherapy in Anaplastic Lymphoma Kinase (ALK)+ Lung Cancer—Current Status and Future Directions. *Transl Lung Cancer Res.* **2023**, *12* (2), 322−336.
(10) Poltavets, A. S.; Vishnyakova, P. A.; Elchaninov, A. V.; Sukhikh, G. T.; Fatkhudinov, T. Kh. Macrophage Modification Strategies for Efficient Cell Therapy. *Cells* **2020**, *9* (6), 1535.
(11) Hirsch, F. R.; Scagliotti, G. V.; Mulshine, J. L.; Kwon, R.; Curran, W. J.; Wu, Y.-L.; Paz-Ares, L. Lung Cancer: Current Therapies and New Targeted Treatments. *Lancet* **2017**, *389* (10066), 299−311.
(12) Bai, R.; Li, L.; Chen, X.; Chen, N.; Song, W.; Cui, J. Neoadjuvant and Adjuvant Immunotherapy: Opening New Horizons for Patients With Early-Stage Non-Small Cell Lung Cancer. *Frontiers Oncol* **2020**, *10*, No. 575472.
(13) Mills, C. D.; Ley, K. M1 and M2Macrophages: The Chicken and the Egg of Immunity. *J. Innate Immun* **2014**, *6* (6), 716−726.

(14) Donovan, A.; Lima, C. A.; Pinkus, J. L.; Pinkus, G. S.; Zon, L. I.; Robine, S.; Andrews, N. C. The Iron Exporter Ferroportin/Slc40a1 Is Essential for Iron Homeostasis. *Cell Metab* **2005**, *1* (3), 191−200.
(15) Vinchi, F.; da Silva, M. C.; Ingoglia, G.; Petrillo, S.; Brinkman, N.; Zuercher, A.; Cerwenka, A.; Tolosano, E.; Muckenthaler, M. U. Hemopexin Therapy Reverts Heme-Induced Proinflammatory Phenotypic Switching of Macrophages in a Mouse Model of Sickle Cell Disease. *Blood* **2016**, *127* (4), 473−486.
(16) Recalcati, S.; Locati, M.; Marini, A.; Santambrogio, P.; Zaninotto, F.; De Pizzol, M.; Zammataro, L.; Girelli, D.; Cairo, G. Differential Regulation of Iron Homeostasis during Human Macrophage Polarized Activation. *Eur. J. Immunol.* **2010**, *40* (3), 824−835.
(17) Recalcati, S.; Gammella, E.; Cairo, G. Ironing out Macrophage Immunometabolism. *Pharm.* **2019**, *12* (2), 94.
(18) Pawate, S.; Shen, Q.; Fan, F.; Bhat, N. R. Redox Regulation of Glial Inflammatory Response to Lipopolysaccharide and Interferon*γ*. *J. Neurosci. Res.* **2004**, *77* (4), 540−551.
(19) Mertens, C.; Marques, O.; Horvat, N. K.; Simonetti, M.; Muckenthaler, M. U.; Jung, M. The Macrophage Iron Signature in Health and Disease. *Int. J. Mol. Sci.* **2021**, *22* (16), 8457.
(20) Fu, H.; Zhang, Z.; Li, D.; Lv, Q.; Chen, S.; Zhang, Z.; Wu, M. LncRNA PELATON, a Ferroptosis Suppressor and Prognositic Signature for GBM. *Frontiers Oncol* **2022**, *12*, No. 817737.
(21) Yano, T.; Obata, Y.; Ishikawa, G.; Ichikawa, T. Enhancing Effect of High Dietary Iron on Lung Tumorigenesis in Mice. *Cancer Lett.* **1994**, *76* (1), 57−62.
(22) Zhao, H.; Tanaka, T.; Mitlitski, V.; Heeter, J.; Balazs, E. A.; Darzynkiewicz, Z. Protective Effect of Hyaluronate on Oxidative DNA Damage in WI-38 and A549 Cells. *Int. J. Oncol.* **2008**, *32* (6), 1159−1167.
(23) Shen, Y.; Li, X.; Zhao, B.; Xue, Y.; Wang, S.; Chen, X.; Yang, J.; Lv, H.; Shang, P. Iron Metabolism Gene Expression and Prognostic Features of Hepatocellular Carcinoma. *J. Cell Biochem* **2018**, *119* (11), 9178−9204.
(24) Torti, S. V.; Torti, F. M. Iron and Cancer: More Ore to Be Mined. *Nat. Rev. Cancer* **2013**, *13* (5), 342−355.
(25) Land, W. G. Transfusion-Related Acute Lung Injury: The Work of DAMPs*. *Transfus Med. Hemoth* **2013**, *40* (1), 3−13.
(26) Nairz, M.; Theurl, I.; Swirski, F. K.; Weiss, G. Pumping Iron"—How Macrophages Handle Iron at the Systemic, Microenvironmental, and Cellular Levels. *Pflugers Arch.* **2017**, *469*, 397−418.
(27) da Silva, M. C.; Breckwoldt, M. O.; Vinchi, F.; Correia, M. P.; Stojanovic, A.; Thielmann, C. M.; Meister, M.; Muley, T.; Warth, A.; Platten, M.; Hentze, M. W.; Cerwenka, A.; Muckenthaler, M. U. Iron Induces Anti-Tumor Activity in Tumor-Associated Macrophages. *Front Immunol* **2017**, *8*, 1479.
(28) Thielmann, C. M.; da Silva, M. C.; Muley, T.; Meister, M.; Herpel, E.; Muckenthaler, M. U. Iron Accumulation in Tumor-Associated Macrophages Marks an Improved Overall Survival in Patients with Lung Adenocarcinoma. *Sci. Rep-uk* **2019**, *9* (1), No. 11326.
(29) Bauer, T. A.; Horvat, N. K.; Marques, O.; Chocarro, S.; Mertens, C.; Colucci, S.; Schmitt, S.; Carrella, L. M.; Morsbach, S.; Koynov, K.; Fenaroli, F.; Blümler, P.; Jung, M.; Sotillo, R.; Hentze, M. W.; Muckenthaler, M. U.; Barz, M. Core Cross-Linked Polymeric Micelles for Specific Iron Delivery: Inducing Sterile Inflammation in Macrophages. *Adv. Healthc Mater.* **2021**, *10*, 2100385.
(30) Schäfer, O.; Huesmann, D.; Barz, M. Poly(S-ethylsulfonyl-l-cysteines) for Chemoselective Disulfide Formation. *Macromolecules* **2016**, *49* (21), 8146−8153.
(31) Klinker, K.; Schäfer, O.; Huesmann, D.; Bauer, T.; Capelôa, L.; Braun, L.; Stergiou, N.; Schinnerer, M.; Dirisala, A.; Miyata, K.; Osada, K.; Cabral, H.; Kataoka, K.; Barz, M. Secondary-Structure-Driven Self-Assembly of Reactive Polypept(o)Ides: Controlling Size, Shape, and Function of Core Cross-Linked Nanostructures. *Angew. Chem., Int. Ed.* **2017**, *56* (32), 9608−9613.
(32) Bauer, T. A.; Schramm, J.; Fenaroli, F.; Siemer, S.; Seidl, C. I.; Rosenauer, C.; Bleul, R.; Stauber, R. H.; Koynov, K.; Maskos, M.; Barz, M. Complex Structures Made Simple − Continuous Flow Production of Core Cross-Linked Polymeric Micelles for Paclitaxel Pro-Drug-Delivery. *Adv. Mater.* **2023**, *35* (21), No. e2210704.
(33) Bauer, T. A.; Imschweiler, J.; Muhl, C.; Weber, B.; Barz, M. Secondary Structure-Driven Self-Assembly of Thiol-Reactive Polypept(o)Ides. *Biomacromolecules* **2021**, *22* (5), 2171−2180.
(34) Schäfer, O.; Klinker, K.; Braun, L.; Huesmann, D.; Schultze, J.; Koynov, K.; Barz, M. Combining Orthogonal Reactive Groups in Block Copolymers for Functional Nanoparticle Synthesis in a Single Step. *ACS Macro Lett.* **2017**, *6* (10), 1140−1145.
(35) Schäfer, O.; Huesmann, D.; Muhl, C.; Barz, M. Rethinking Cysteine Protective Groups: S-Alkylsulfonyl-L-cysteines for Chemoselective Disulfide Formation. *Chem.—Eur. J.* **2016**, *22* (50), 18085−18091.
(36) Schlüter, C.; Duchrow, M.; Wohlenberg, C.; Becker, M. H.; Key, G.; Flad, H. D.; Gerdes, J. The Cell Proliferation-Associated Antigen of Antibody Ki-67: A Very Large, Ubiquitous Nuclear Protein with Numerous Repeated Elements, Representing a New Kind of Cell Cycle-Maintaining Proteins. *J. Cell Biol.* **1993**, *123* (3), 513−522.
(37) Rogakou, E. P.; Pilch, D. R.; Orr, A. H.; Ivanova, V. S.; Bonner, W. M. DNA Double-Stranded Breaks Induce Histone H2AX Phosphorylation on Serine 139*. *J. Biol. Chem.* **1998**, *273* (10), 5858−5868.
(38) Butler, L. M.; Zhou, X.; Xu, W.-S.; Scher, H. I.; Rifkind, R. A.; Marks, P. A.; Richon, V. M. The Histone Deacetylase Inhibitor SAHA Arrests Cancer Cell Growth, up-Regulates Thioredoxin-Binding Protein-2, and down-Regulates Thioredoxin. *Proc. National Acad. Sci.* **2002**, *99* (18), 11700−11705.
(39) Cai, B.; Kasikara, C.; Doran, A. C.; Ramakrishnan, R.; Birge, R. B.; Tabas, I. MerTK Signaling in Macrophages Promotes the Synthesis of Inflammation Resolution Mediators by Suppressing CaMKII Activity. *Sci. Signal* **2018**, *11* (549), na DOI: 10.1126/scisignal.aar3721.
(40) MULERO, V.; WEI, X.; LIEW, F. Y.; BROCK, J. H. Regulation of Phagosomal Iron Release from Murine Macrophages by Nitric Oxide. *Biochem. J.* **2002**, *365* (1), 127−132.
(41) Aldrovandi, M.; Conrad, M. Ferroptosis: The Good, the Bad and the Ugly. *Cell Res.* **2020**, *30* (12), 1061−1062.
(42) Lemaire, G.; Alvarez-Pachon, F.-J.; Beuneu, C.; Lepoivre, M.; Petit, J.-F. Differential Cytostatic Effects of NO Donors and NO Producing Cells. *Free Radical Bio Med.* **1999**, *26* (9−10), 1274−1283.
(43) Van den Bossche, J.; Baardman, J.; Otto, N. A.; van der Velden, S.; Neele, A. E.; van den Berg, S. M.; Luque-Martin, R.; Chen, H.-J.; Boshuizen, M.; Ahmed, M.; Hoeksema, M. A.; de Vos, A. F.; de Winther, M. Mitochondrial Dysfunction Prevents Repolarization of Inflammatory Macrophages. *Cell Reports* **2016**, *17* (3), 684−696.
(44) Maddalo, D.; Manchado, E.; Concepcion, C. P.; Bonetti, C.; Vidigal, J. A.; Han, Y.-C.; Ogrodowski, P.; Crippa, A.; Rekhtman, N.; de Stanchina, E.; Lowe, S. W.; Ventura, A. In Vivo Engineering of Oncogenic Chromosomal Rearrangements with the CRISPR/Cas9 System. *Nature* **2014**, *516*, 423−427.
(45) da Silva, M. C.; Breckwoldt, M. O.; Vinchi, F.; Correia, M. P.; Stojanovic, A.; Thielmann, C. M.; Meister, M.; Muley, T.; Warth, A.; Platten, M.; Hentze, M. W.; Cerwenka, A.; Muckenthaler, M. U. Iron Induces Anti-Tumor Activity in Tumor-Associated Macrophages. *Front Immunol* **2017**, *8*, 1479.
(46) Scagliotti, G.; Stahel, R. A.; Rosell, R.; Thatcher, N.; Soria, J.-C. ALK Translocation and Crizotinib in Non-Small Cell Lung Cancer: An Evolving Paradigm in Oncology Drug Development. *Eur. J. Cancer* **2012**, *48* (7), 961−973.
(47) Shrestha, N.; Nimick, M.; Dass, P.; Rosengren, R. J.; Ashton, J. C. Mechanisms of Suppression of Cell Growth by Dual Inhibition of ALK and MEK in ALK-Positive Non-Small Cell Lung Cancer. *Sci. Rep-uk* **2019**, *9* (1), No. 18842.
(48) Guo, Q.; Liu, L.; Chen, Z.; Fan, Y.; Zhou, Y.; Yuan, Z.; Zhang, W. Current Treatments for Non-Small Cell Lung Cancer. *Frontiers Oncol* **2022**, *12*, No. 945102.
(49) Zanganeh, S.; Hutter, G.; Spitler, R.; Lenkov, O.; Mahmoudi, M.; Shaw, A.; Pajarinen, J. S.; Nejadnik, H.; Goodman, S.; Moseley, M.; Coussens, L. M.; Daldrup-Link, H. E. Iron Oxide Nanoparticles Inhibit

Tumour Growth by Inducing Pro-Inflammatory Macrophage Polarization in Tumour Tissues. *Nat. Nanotechnol* **2016**, *11* (11), 986−994.
(50) Cameron, D. J.; Churchill, W. H. Cytotoxicity of Human Macrophages for Tumor Cells. Enhancement by Human Lymphocyte Mediators. *J. Clin Invest* **1979**, *63* (5), 977−984.
(51) Hudson, S. V.; Miller, H. A.; Mahlbacher, G. E.; Saforo, D.; Beverly, L. J.; Arteel, G. E.; Frieboes, H. B. Computational/Experimental Evaluation of Liver Metastasis Post Hepatic Injury: Interactions with Macrophages and Transitional ECM. *Sci. Rep-uk* **2019**, *9* (1), No. 15077.
(52) Bartha, L.; Eftimie, R. Mathematical Investigation into the Role of Macrophage Heterogeneity on the Temporal and Spatio-Temporal Dynamics of Non-Small Cell Lung Cancers. *J. Theor. Biol.* **2022**, *549*, No. 111207.
(53) Li, X.; Jolly, M. K.; George, J. T.; Pienta, K. J.; Levine, H. Computational Modeling of the Crosstalk Between Macrophage Polarization and Tumor Cell Plasticity in the Tumor Microenvironment. *Frontiers Oncol* **2019**, *9*, 10.
(54) Hegedűs, C.; Kovács, K.; Polgár, Z.; Regdon, Z.; Szabó, É.; Robaszkiewicz, A.; Forman, H. J.; Martner, A.; Virág, L. Redox Control of Cancer Cell Destruction. *Redox Biol.* **2018**, *16*, 59−74.
(55) Kim, S. J.; Kim, H. S.; Seo, Y. R. Understanding of ROS-Inducing Strategy in Anticancer Therapy. *Oxid Med. Cell Longev* **2019**, *2019*, No. 5381692.
(56) Wang, K.; Jiang, J.; Lei, Y.; Zhou, S.; Wei, Y.; Huang, C. Targeting Metabolic−Redox Circuits for Cancer Therapy. *Trends Biochem. Sci.* **2019**, *44* (5), 401−414.
(57) Teppo, H.-R.; Soini, Y.; Karihtala, P. Reactive Oxygen Species-Mediated Mechanisms of Action of Targeted Cancer Therapy. *Oxid Med. Cell Longev* **2017**, *2017*, No. 1485283.
(58) Samarin, J.; Fabrowski, P.; Kurilov, R.; Nuskova, H.; Hummel-Eisenbeiss, J.; Pink, H.; Li, N.; Weru, V.; Alborzinia, H.; Yildiz, U.; Grob, L.; Taubert, M.; Czech, M.; Morgen, M.; Brandstädter, C.; Becker, K.; Mao, L.; Jayavelu, A. K.; Goncalves, A.; Uhrig, U.; Seiler, J.; Lyu, Y.; Diederichs, S.; Klingmüller, U.; Muckenthaler, M.; Kopp-Schneider, A.; Teleman, A.; Miller, A. K.; Gunkel, N. Low Level of Antioxidant Capacity Biomarkers but Not Target Overexpression Predicts Vulnerability to ROS-Inducing Drugs. *Redox Biol.* **2023**, *62*, No. 102639.
(59) Wang, Y.; Zhang, X.; Yang, L.; Xue, J.; Hu, G. Blockade of CCL2 Enhances Immunotherapeutic Effect of Anti-PD1 in Lung Cancer. *J. Bone Oncol* **2018**, *11*, 27−32.
(60) Binnewies, M.; Roberts, E. W.; Kersten, K.; Chan, V.; Fearon, D. F.; Merad, M.; Coussens, L. M.; Gabrilovich, D. I.; Ostrand-Rosenberg, S.; Hedrick, C. C.; Vonderheide, R. H.; Pittet, M. J.; Jain, R. K.; Zou, W.; Howcroft, T. K.; Woodhouse, E. C.; Weinberg, R. A.; Krummel, M. F. Understanding the Tumor Immune Microenvironment (TIME) for Effective Therapy. *Nat. Med.* **2018**, *24* (5), 541−550.
(61) Zeisberger, S. M.; Odermatt, B.; Marty, C.; Zehnder-Fjällman, A. H. M.; Ballmer-Hofer, K.; Schwendener, R. A. Clodronate-Liposome-Mediated Depletion of Tumour-Associated Macrophages: A New and Highly Effective Antiangiogenic Therapy Approach. *Br. J. Cancer* **2006**, *95* (3), 272−281.
(62) Gubin, M. M.; Esaulova, E.; Ward, J. P.; Malkova, O. N.; Runci, D.; Wong, P.; Noguchi, T.; Arthur, C. D.; Meng, W.; Alspach, E.; Medrano, R. F. V.; Fronick, C.; Fehlings, M.; Newell, E. W.; Fulton, R. S.; Sheehan, K. C. F.; Oh, S. T.; Schreiber, R. D.; Artyomov, M. N. High-Dimensional Analysis Delineates Myeloid and Lymphoid Compartment Remodeling during Successful Immune-Checkpoint Cancer Therapy. *Cell* **2018**, *175* (4), 1014−1030.
(63) Giordano, S.; Petrelli, A. From Single- to Multi-Target Drugs in Cancer Therapy: When Aspecificity Becomes an Advantage. *Curr. Med. Chem.* **2008**, *15* (5), 422−432.
(64) Bedard, P. L.; Hyman, D. M.; Davids, M. S.; Siu, L. L. Small Molecules, Big Impact: 20 Years of Targeted Therapy in Oncology. *Lancet* **2020**, *395* (10229), 1078−1088.
(65) Greten, F. R.; Grivennikov, S. I. Inflammation and Cancer: Triggers, Mechanisms, and Consequences. *Immunity* **2019**, *51* (1), 27−41.
(66) Ries, C. H.; Cannarile, M. A.; Hoves, S.; Benz, J.; Wartha, K.; Runza, V.; Rey-Giraud, F.; Pradel, L. P.; Feuerhake, F.; Klaman, I.; Jones, T.; Jucknischke, U.; Scheiblich, S.; Kaluza, K.; Gorr, I. H.; Walz, A.; Abiraj, K.; Cassier, P. A.; Sica, A.; Gomez-Roca, C.; de Visser, K. E.; Italiano, A.; Le Tourneau, C.; Delord, J.-P.; Levitsky, H.; Blay, J.-Y.; Rüttinger, D. Targeting Tumor-Associated Macrophages with Anti-CSF-1R Antibody Reveals a Strategy for Cancer Therapy. *Cancer Cell* **2014**, *25* (6), 846−859.
(67) Muzumdar, M. D.; Tasic, B.; Miyamichi, K.; Li, L.; Luo, L. A Global Double-fluorescent Cre Reporter Mouse. *Genesis* **2007**, *45* (9), 593−605.
(68) Oikonomou, N.; Mouratis, M.-A.; Tzouvelekis, A.; Kaffe, E.; Valavanis, C.; Vilaras, G.; Karameris, A.; Prestwich, G. D.; Bouros, D.; Aidinis, V. Pulmonary Autotaxin Expression Contributes to the Pathogenesis of Pulmonary Fibrosis. *Am. J. Resp Cell Mol.* **2012**, *47* (5), 566−574.
(69) Guida, C.; Altamura, S.; Klein, F. A.; Galy, B.; Boutros, M.; Ulmer, A. J.; Hentze, M. W.; Muckenthaler, M. U. A Novel Inflammatory Pathway Mediating Rapid Hepcidin-Independent Hypoferremia. *Blood* **2015**, *125* (14), 2265−2275.
(70) Hodgkin, P. D.; Lee, J. H.; Lyons, A. B. B Cell Differentiation and Isotype Switching Is Related to Division Cycle Number. *J. Exp Medicine* **1996**, *184* (1), 277−281.
(71) Müller, T.; Kalxdorf, M.; Longuespée, R.; Kazdal, D. N.; Stenzinger, A.; Krijgsveld, J. Automated Sample Preparation with SP3 for Low-input Clinical Proteomics. *Mol. Syst. Biol.* **2020**, *16* (1), No. e9111.
(72) Heming, S.; Hansen, P.; Vlasov, A.; Schwörer, F.; Schaumann, S.; Frolovaitė, P.; Lehmann, W.-D.; Timmer, J.; Schilling, M.; Helm, B.; Klingmüller, U. MSPypeline: A Python Package for Streamlined Data Analysis of Mass Spectrometry-Based Proteomics. *Bioinform Adv.* **2022**, *2* (1), na DOI: 10.1093/bioadv/vbac004.
(73) Ritchie, M. E.; Phipson, B.; Wu, D.; Hu, Y.; Law, C. W.; Shi, W.; Smyth, G. K. Limma Powers Differential Expression Analyses for RNA-Sequencing and Microarray Studies. *Nucleic Acids Res.* **2015**, *43* (7), e47−e47.
(74) Zhou, Y.; Zhou, B.; Pache, L.; Chang, M.; Khodabakhshi, A. H.; Tanaseichuk, O.; Benner, C.; Chanda, S. K. Metascape Provides a Biologist-Oriented Resource for the Analysis of Systems-Level Datasets. *Nat. Commun.* **2019**, *10* (1), 1523.
(75) Torrance, J. D.; Bothwell, T. H. A Simple Technique for Measuring Storage Iron Concentrations in Formalinised Liver Samples. *South Afr J. Medical Sci.* **1968**, *33* (1), 9−11.
(76) Stirling, D. R.; Swain-Bowden, M. J.; Lucas, A. M.; Carpenter, A. E.; Cimini, B. A.; Goodman, A. CellProfiler 4: Improvements in Speed, Utility and Usability. *Bmc Bioinformatics* **2021**, *22* (1), 433.
(77) Vizcaíno, J. A.; Côté, R. G.; Csordas, A.; Dianes, J. A.; Fabregat, A.; Foster, J. M.; Griss, J.; Alpi, E.; Birim, M.; Contell, J.; O'Kelly, G.; Schoenegger, A.; Ovelleiro, D.; Pérez-Riverol, Y.; Reisinger, F.; Ríos, D.; Wang, R.; Hermjakob, H. The Proteomics Identifications (PRIDE) Database and Associated Tools: Status in 2013. *Nucleic Acids Res.* **2012**, *41* (D1), D1063−D1069.

https://doi.org/10.1021/acsnano.3c08335
ACS Nano 2024, 18, 11025−11041